Multispectral analysis of Northern Hemisphere temperature records over the last five millennia

C. Taricco · S. Mancuso · F. C. Ljungqvist · S. Alessio · M. Ghil

Abstract Aiming to describe spatio-temporal climate variability on decadal-to-centennial time scales and longer, we analyzed a data set of 26 proxy records extending back 1,000–5,000 years; all records chosen were calibrated to yield temperatures. The seven irregularly sampled series in the data set were interpolated to a regular grid by optimized methods and then two advanced spectral methods—namely singular-spectrum analysis (SSA) and the continuous wavelet transform—were applied to individual series to separate significant oscillations from the high noise background. This univariate analysis identified several common periods across many of the 26 proxy records: a millennial trend, as well as oscillations of about 100 and 200 years, and a broad peak in the 40–70-year band. To study common NH oscillations, we then applied Multichannel SSA. Temperature variations on time scales longer than 600 years appear in our analysis as a dominant trend component, which shows climate features consistent with the Medieval Warm Period and the Little Ice Age. Statistically significant NH-wide peaks appear at 330, 250 and 110 years, as well as in a broad 50–80-year band. Strong variability centers in several bands are located around the North Atlantic basin and are in phase opposition between Greenland and Western Europe.

C. Taricco (✉) · S. Alessio
Dipartimento di Fisica, Università di Torino, Turin, Italy
e-mail: carla.taricco@unito.it

C. Taricco · S. Mancuso · S. Alessio
INAF – Osservatorio Astrofisico di Torino, Pino Torinese, Italy

F. C. Ljungqvist
Department of History, Stockholm University, Stockholm, Sweden

F. C. Ljungqvist
Bolin Centre for Climate Research, Stockholm University, Stockholm, Sweden

M. Ghil
Geosciences Department and Laboratoire de Météorologie Dynamique (CNRS and IPSL), École Normale Supérieure, Paris, France

M. Ghil
Department of Atmospheric and Oceanic Sciences and Institute of Geophysics and Planetary Physics, University of California, Los Angeles, CA, USA

1 Introduction and motivation

Recent years have seen significant progress in understanding late Holocene spatial and temporal climate variability thanks to new studies based on different proxy types, including tree-ring width and density records, along with $\delta^{18}O$ in ice cores, terrestrial and marine sediment records, as well as in speleothems (Wanner et al. 2008; Ljungqvist et al. 2012; PAGES 2k Consortium 2013). Progress has also been achieved by comparing and integrating information from proxy data with simulations from global climate models (Masson-Delmotte et al. 2013; Fernández-Donado et al. 2013; Moberg 2013).

Many analyses of the last one-to-two millennia rely on large sets of records coming from different types of proxies. These analyses often provide multi-proxy temperature reconstructions on a hemispheric or global scale, although they are usually heavily biased towards tree-ring width

records [e.g., Mann et al. 2009]. In the attempt to collect as many series as possible, one must, however, avoid insufficiently careful temperature calibration of the proxy data (Tingley et al. 2012). The difficulties in transforming proxy data into quantitative temperature series are numerous and depend on the type of proxy—whether obtained from tree rings, speleothems or ice cores—and they are also related to the region from which the proxy comes, in particular to its climate type.

For this reason, our data set contains only series with at least decadal resolution, which satisfy in addition the requirement that the temperature calibration of each proxy record be provided by the authors who published the record itself. Støve et al. (2012) discussed at length the way that parametric and nonparametric, as well as linear and non-linear, transfer functions between one or more proxies and a single climate variable, like temperature, can be applied and calibrated. This multiplicity of possible calibrations makes it that much more desirable to rely on the familiarity of the record's original authors with the local and regional characteristics of the proxy. Moreover, in order to be able to study in a reliable way multi-decadal to centennial variability, we only considered series that extend back at least to AD 1000.

An important point of our work is that we try to preserve the regional information carried by each time series, not only by using single-series spectral methods but also by applying a multivariate method. This dual approach, supported by a robust spectral analysis, differentiates our work from other recent studies aimed at distinguishing among regional expressions of past global climate changes; see, for instance PAGES 2k Consortium (2013). Thus, our aim is not to use our data set to produce an averaged multi-proxy temperature series for the Northern Hemisphere (NH) but to look for common modes of variability, as well as for differences among geographical areas.

For the single-record analyses we use two advanced spectral methods—singular spectrum analysis [SSA: Vautard and Ghil 1989; Ghil et al. 2002] and the continuous wavelet transform [(CWT: Torrence and Compo 1998]—while for the multi-record analyses we use multichannel SSA [MSSA: Keppenne and Ghil 1993; Plaut and Vautard 1994]. Both SSA-based methods and wavelet-based methods have been used already extensively in the paleoclimate, as well as in the modern-climate literature (Ghil et al. 2002).

In fact, paleoclimate applications motivated to a large extent the original development of SSA as a spectral method (Vautard and Ghil 1989), while MSSA has already been used by Jiang et al. (1995) to study the spatio-temporal patterns of the sea surface temperature (SST) and zonal wind fields associated with the El Niño–Southern Oscillation, by Unal and Ghil (1995) to investigate sea surface height variations from tide gauge records, and by Moron et al. (1998) to analyze global SST variations over the twentieth century, among many others. We refer the interested reader to the "Appendix" and to the references for technical details.

This paper is organized as follows: Sect. 2 describes the data set; Sect. 3 presents the results of SSA and CWT, performed on single time series; while Sect. 4 provides the MSSA results. Concluding remarks follow in Sect. 5, and the spectral methods employed in Sects. 3 and 4 are described in the "Appendix".

2 The proxy data set and its pre-processing

2.1 The data set

As mentioned above, the proxy records that we selected for our analysis were calibrated to temperature by the authors who published the records themselves and, in addition, had time coverage that extended back to at least AD 1000. All the records retained are from the extratropical NH.

The data set so obtained contains 19 regularly spaced time series, mostly with a sampling interval of $\Delta t = 1$ year, and seven irregularly spaced time series. The geographic distribution of the 26 time-series is shown in Fig. 1 and their properties are listed in Table 5. Figure 2 allows us to compare the different lengths of the series, which are ordered by increasing latitude and whose amplitude is plotted in arbitrary units. This data set has been analyzed by single-series spectral methods (SSA and CWT), in Sect. 3, as well as by MSSA, in Sect. 4; in both approaches, uniformly spaced time series are needed. Therefore, we pre-processed the seven irregularly spaced proxy records as described in the next subsection.

All quantitative temperature proxy records—extending back to at least AD 1000 and calibrated by their original authors—that were available to us by June 2012 were included. Some records were available to us in digital form but only as standardized values and not as temperature-calibrated reconstructions, e.g., the Taimyr tree-ring width record of Naurzbaev et al. (2002) and the Mongolian tree-ring width record of D'Arrigo et al. (2001); these, too, were excluded. Moreover, we only gained access to the last 1,000 years of the 2,485-year–long tree-ring width temperature reconstruction from the central-eastern Tibetan Plateau (Liu et al. 2009). In order to increase the spatial coverage, we included two regional multi-proxy composites of annual mean temperature in our data set: the Russian Plains record of Sleptsov and Klimenko (2003) and the whole-China reconstruction of Yang et al. (2002).

These proxy records have different spectral biases, since not all proxy types can capture the variability on all time
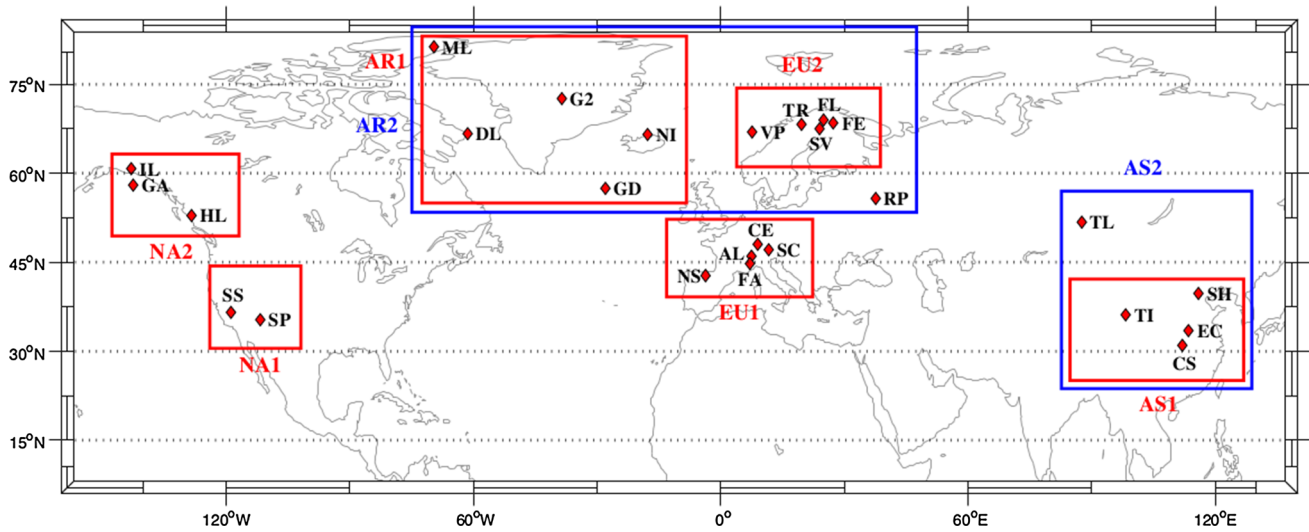
Fig. 1 World map showing the location of the 26 proxy records in our study. The *rectangles* indicate groups of records that were used in the regional multichannel analysis described in Sect. 4. Please see Table 5 for a summary description of each record. The regions are labeled AR1, AR2, ..., NA2, as described in Table 3 of Sect. 4

Fig. 2 Time coverage of the 26 proxy records in our data set. The records are identified by the *two-letter acronyms* introduced in Table 5 and they have been centered to zero mean and normalized to unit variance; the *different colors* represent latitude belts, namely 30–60°N (*orange*), 60–90°N (*green*)
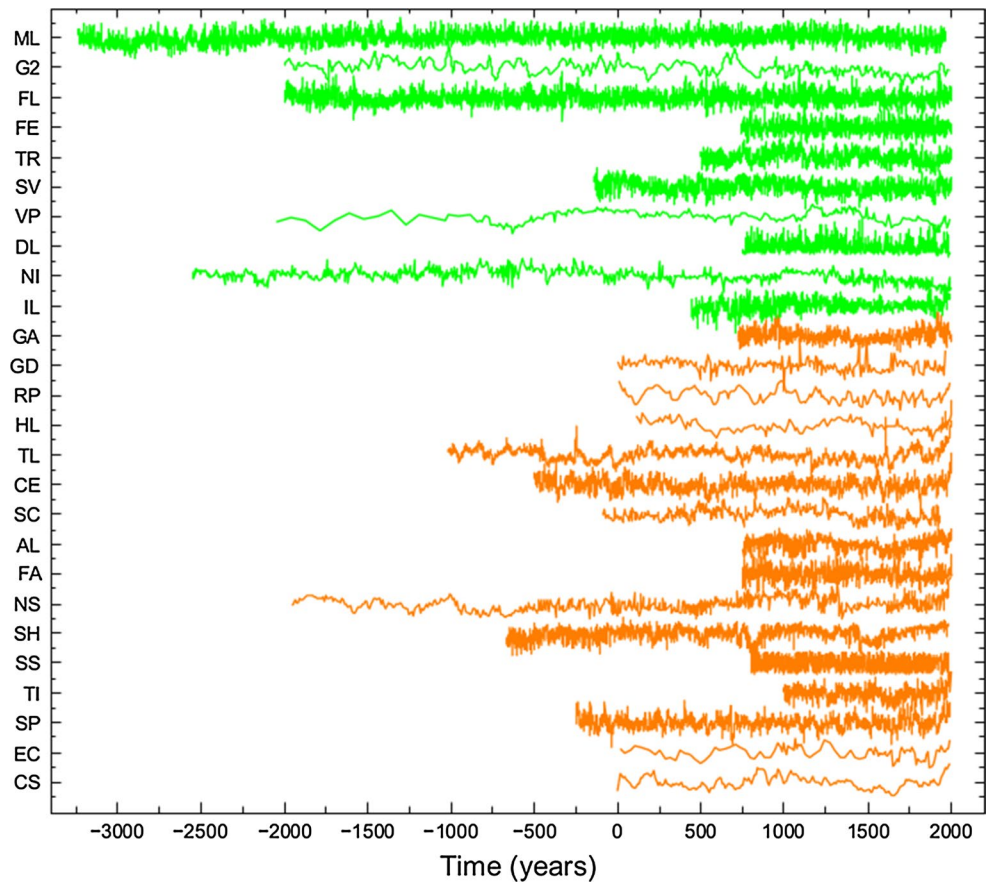
scales equally well. Records with less-than-annual resolution cannot capture variability on an interannual and possibly decadal time scale. Tree-ring records might have certain limitations when it comes to preserving the variability

at very low, multi-centennial to millennial frequencies, cf. Cook et al. (1995). Tree-ring records of maximum density seem to represent better temperature variability at both high and low frequencies than tree-ring width records (Franke

et al. 2013). Maximum-density records also have, in general, much higher correlation r with temperature than ring-width records—typically $r \sim 0.7$ versus ~ 0.4—and over a longer seasonal window (Briffa et al. 2002).

Several proxy records in our data set are derived from other types of archives than tree rings or historical documentary records, and are affected by dating uncertainties. The uncertainty is often difficult to quantify; the estimate for the Donard Lake varved sediment record (Moore et al. 2001) is up to ±20 years; for the Lower Murray Lake varved sediment record (Cook et al. 2009) it is ±16 years; for the Iceberg Lake varved sediment record (Loso 2009) it is ±32 years; for the Shi Hua Cave speleothem layer thickness record (Tan et al. 2003) it is ±5 years. Moreover, the age model in the Hallet Lake sediment record (McKay et al. 2008) is insufficiently constrained and hence it contains significant uncertainties.

Some of the temperature proxy records were already spectrally analyzed by their original authors or in subsequent studies. Tan et al. (2003) identified peaks of about 206 and 325 years in their Shi Hua Cave speleothem record. Martín-Chivelet et al. (2011) found oscillations of about 440, 900 and 1,300 years in their speleothem $\delta^{13}C$ record from Northern Spain. Salzer and Kipfmueller (2005) used the Blackman-Tukey method to find in their Southern Colorado Plateau tree-ring width record, oscillations of about 41 and 178 years. Using the 2,485-year–long temperature reconstruction of Liu et al. (2009), based on tree-ring widths from the central-eastern Tibetan Plateau, Liu et al. (2011) identified significant cycles of 110, 199, 800 and 1,324 years.

In the Gulf of Alaska tree-ring width record, Wilson et al. (2007) identified cycles of 10–11, 13–14 and 18–19 years by applying the multi-taper method of Mann and Lees (1996) and cycles of 18.7, 50.4, 38.0, 91.8, 24.4, 15.3 and about 150 years by using SSA, as we shall do here. The multi-taper method also yielded spectral peaks of about 225, 135 and 105 years in the Finnish Lapland tree-ring width record of Helama and Macias Fauria (2010). Lindholm and Jalkanen (2012) found periodicities of 33, 23 and 11 years in a Fourier spectrum of their Fennoscandian (Laanila) tree-ring height-increment record (Lindholm et al. 2011) and a Morlet wavelet spectrum thereof. Sicre et al. (2008, 2011) identified spectral peaks of 50–150 and 20–25 years in their $U_K^{37'}$ alkenone-based sea surface temperature reconstruction from the North Icelandic Shelf, by means of a Morlet wavelet analysis and by the multi-taper method.

These studies on single series have thus obtained a substantial number of decadal-scale and lower-frequency peaks. These results, however, were obtained by using spectral-analysis methods different from series to series. In order to obtain a more reliable and robust analysis of

the entire set, we decided to analyze all the records, one by one, by using the two complementary methods of SSA and CWT, accompanied by stringent tests of statistical significance.

2.2 Pre-processing the unevenly sampled time series

In order to apply SSA and CWT, we had to transform the seven unevenly sampled series—measured at irregular times $t_1, t_2, \ldots, t_N$—into evenly spaced series, by means of data interpolation onto a uniform grid. For each record, we chose the optimal regular sampling time Δt_*, by requiring that the spectrum of the synthesized evenly spaced series be as similar as possible to the spectrum of the original series. For each record, we considered the full time span $t_{span} = t_N - t_1$, except for the Vøring Plateau foraminiferic record (see Table 5), whose earlier parts were discarded due to their exceedingly sparse sampling. In order to explore the full range of variability on all time scales in the data, no trends were removed prior to data processing.

The Lomb-Scargle periodogram (Lomb 1976; Scargle 1982; MacDonald 1989) is a common tool in the spectral analysis of unequally spaced data. This method is equivalent to a linear least-squares fit of a sum of sine and cosine functions to the observed time series, and it can be applied to both unevenly and evenly spaced data: when the data are regularly spaced, it is analogous to a Fourier analysis.

Hocke and Kämpfer (2009) proposed an approach for dealing with unevenly sampled data in the time domain, based on the Lomb-Scargle periodogram. We did not adopt their approach here, however, for two reasons: first, as the above authors themselves concluded, the proposed algorithm does not perform in a robust and reliable way; and second, their algorithm does not provide the optimal sampling interval, given the unevenly sampled data.

We proceeded instead as follows, for each individual time series:

- (i) calculate the Lomb-Scargle periodogram LS^{irr} of the original, irregular record;
- (ii) resample the irregular series at regular sampling intervals Δt^{reg} in a plausible range (say, between 1 and 30 years in steps of 0.01 year);
- (iii) calculate for each Δt^{reg} the corresponding periodogram LS^{reg};
- (iv) identify the LS^{reg} that best reproduces the features of LS^{irr}, say LS^{reg}_*; and
- (v) choose the corresponding Δt_* as the optimal sampling time for the interpolation.
- The vicinity of each LS^{reg} to LS^{irr} was quantified by the root-mean-squared error (RMSE): Assume that we sample both LS^{irr} and LS^{reg} at N' frequencies $f_i = f_1, \ldots, f'_N$,

Table 1 Uniform spacing of the seven irregularly sampled time series: Δt_* is the sampling interval obtained as explained in the text, and N is the number of samples in each evenly spaced series

Acronym	Interpolation method	Δt_* (year)	N
EC	Linear	18.17	109
NS	Linear	6.10	648
SC	Cubic spline	3.13	647
HL	Cubic spline	13.27	143
GD	Linear	8.97	220
NI	Linear	4.47	1018
VP (883 BC–1995 AD)	Cubic spline	10.86	266

and choose LS_*^{reg} as the one that minimizes the square root of the sum of the squares of the residuals divided by the number N' of comparison frequencies. The RMSE R is thus defined, as usual, by

$$R = \left\{ \frac{\sum_i (LS^{\text{irr}}(f_i) - LS^{\text{reg}}(f_i))^2}{N'} \right\}^{1/2}. \tag{1}$$

To produce the evenly spaced time series, we used both linear and cubic-spline interpolations. We recall that, in linear interpolation, the data is fitted by a straight line in the Δt interval between each pair of data points, also called nodes; therefore the resulting curves are continuous but their first derivative may be discontinuous at each node.

Cubic-spline interpolation fits instead a cubic polynomial over each subinterval; the fitted interpolation curve is piecewise cubic, with (at least) two continuous derivatives at the nodes; in this way, it is possible to obtain a smoother interpolated curve. Cubic splines, however, produce curves that often have overshoots and need, therefore, to be carefully checked for the accuracy of their fit to the data. The question of which of the two interpolation methods, linear or cubic, is the most appropriate in each specific case was dealt with by determining which of the two methods provides the best spectral match with respect to LS^{irr}.

In summary, for each time series and for each of the two interpolation methods, we calculated a set of spectra LS^{reg} for many values of Δt, varying from 1 to 30 years, and the respective RMSE values R, by comparing each LS^{reg} with the original LS^{irr}, taken as the reference periodogram. The results were expressed graphically as curves of R versus Δt. Finally, the optimum sampling interval Δt_* was chosen as the one that gives the best spectral match, corresponding to the minimum value R^* of R.

Table 1 summarizes the results of this procedure, and gives the interpolation method chosen for each series, the optimal sampling interval Δt_* and the number of samples N of the interpolated series. The sampling interval optimization applies to those time series that, to start with, are irregular but have no gaps, as well as to those that were regularly spaced but had gaps.

As is customary when no a priori information is available, we assume stationarity of the time series in the following analysis, but point out that SSA has proven quite efficient at capturing linear, as well as nonlinear, data-adaptive trends (Ghil et al. 2002 and references therein), while CWT is specifically designed to capture frequency modulation of a signal, cf. Torrence and Compo (1998) and the entire wavelet literature.

3 Analysis of single records

On each of the 26 time series—now all uniformly spaced—we performed spectral analysis by SSA and CWT. When the length of the series allowed it, we used for SSA a window length of 600 years, in order to be able to reliably detect multi-decadal and even lower-frequency cycles, without missing possible decadal variations. The Monte Carlo significance tests are performed at the 99 % confidence level, unless otherwise stated.

In SSA, oscillatory modes are captured by a pair of nearly equal eigenvalues of the lag-covariance matrix, and by the associated eigenvectors: the eigenvalues correspond to variances in the phase-space directions given by the eigenvectors, as explained in the "Appendix" here and in the references (Vautard and Ghil 1989; Vautard et al. 1992; Ghil et al. 2002).

As for CWT, all series were analyzed by using a Morlet complex wavelet with parameter $\omega_0 = 6$ as the mother wavelet (or generating function), and significance tests were run according to the guidelines suggested by Torrence and Compo (1998). We refer the interested reader to the "Appendix" for technical details on both SSA and CWT.

The highly significant periodicities found by one or both methods in the individual series are reported in Table 6. Unless noted otherwise, all oscillations in the table are significant at the 99 % level and above. Only a few of the periodicities in the table are significant at the 95 % or the 90 % level; the corresponding significance level is indicated in parentheses next to the periodicity.

The range of detected oscillations has been divided into three classes: (a) decadal and multidecadal, of about 10, 20–30, and 40–70 years; (b) centennial and multi-centennial, of about 100, 200, 300, 400, and 500–700 years; and (c) a millennial trend.

Several common periods have been found: in particular, the majority of the series show a millennial trend, with a time scale longer than 800 years, as well as oscillations of about 100 and 200 years, along with a broad peak in the 40–70-year band. The millennial trend is present in all but
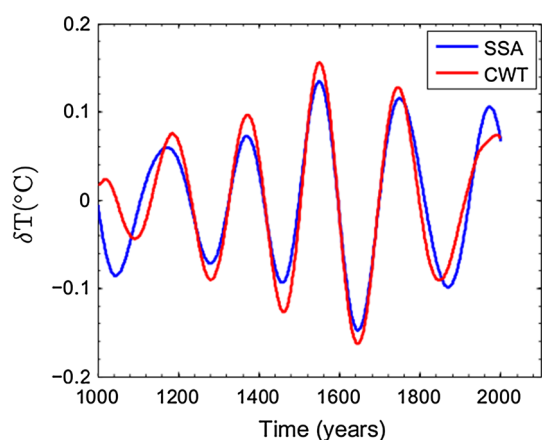
Fig. 3 Example of agreement between reconstructions by SSA and CWT: the 200-year oscillation in the central-eastern Tibetan Plateau tree-ring width record of Liu et al. (2009)

three of the 26 time series, and it is significant at the 99 % level in both methods for 15 series.

We also notice an 11-year cycle appearing in five of the proxy records, in either SSA only (two records—SV and NI) or both SSA and CWT (three records—FE, GA and SS). Four of the five proxy records that exhibit a significant 11-year signal are regularly sampled and have a sampling interval of 1 year (FE, SV, GA and SS; see Table 5). Only NI had an irregular sampling rate with an average sampling interval of 4.47 years; the 11-year oscillation is only significant in the SSA results.

The periods of the oscillations detected by both spectral methods are highlighted in bold in Table 6. In these cases, we verified that the amplitude and phase of the oscillations reconstructed separately by SSA and by CWT, and not only the frequencies, are in agreement. An example of this situation is illustrated in Fig. 3 for the ∼200 years oscillations of the central-eastern Tibetan Plateau tree-ring width series.

As expected (Lindholm et al. 2011), we notice that the Fennoscandian tree-ring height increment record shows only sub-centennial variability. Likewise, the Southern Sierra Nevada tree-ring width record (Graumlich 1993) was studied and published prior to the Regional Curve Standardization (RCS) method and thus its low-frequency signal may be strongly damped.

4 Multichannel-SSA (MSSA) results

4.1 The last millennium: reconstructed variability

The temperature proxy records under study have a considerable range of temporal coverage; see Fig. 2, as well as Tables 1 and 5. We thus applied MSSA to the entire data set over the largest-possible common interval, spanning

AD 1000 to AD 1935. Prior to the analysis, all the time series were interpolated to a common annual resolution, as described in Sect. 2.2. Furthermore, to avoid the dominance of variability in one or several channels, each time series was centered to have zero mean and unit variance (Plaut and Vautard 1994; Shabalova and Weber 1998; Ghil et al. 2002).

In this way, we obtained a homogeneous data set with $L = 26$ spatial channels and a common length of $N = 936$ years. No other filtering or detrending was applied to the data, and the statistically significant oscillations were scaled back up to present the results as temperature variations in °C for each time series.

Selecting the window length M for MSSA—like for single-channel SSA—involves a trade-off between the amount of spectral information, such as the number of peaks, one may gain on the time series, on the one hand, and the degree of signal-to-noise enhancement and the associated statistical confidence, on the other. The choice of M corresponds, therewith, to a compromise between including more peaks for larger M—while taking into account that periods longer than M cannot be resolved—and achieving a higher degree of statistical significance for the peaks detected, at smaller M.

In general, the stable features of the eigenset—i.e., of the set of eigenvalues and eigenvectors—can be evaluated by varying the window size M over a given range, $M_1 \leq M \leq M_2$. Since the use of a given M allows the identification of oscillations with periods that do not exceed M (Vautard et al. 1992), we expect to identify, accurately and reliably, periods up to 300 years from data spanning the last millennium.

Vautard and Ghil (1989) recommended to choose M no larger than ∼ $N/3$, with N the length of the data set. Therefore, we use here a standard window length of $M = 300$ years $\leq N/3 = 312$ years. In this way, we obtain spatio-temporal principal components (ST-PCs) of length $N' = N - M + 1 = 637$ years; see the "Appendix" for details on the spectral methods.

The MSSA singular spectrum (not shown) includes several pairs of eigenvalues that are approximately equal and whose error bars overlap, while the long-term trend is captured by a single eigenvalue. These pairs may represent significant oscillations, but statistical tests are required to quantify significance.

The Monte Carlo test for MSSA of Allen and Robertson (1996) was thus applied in order to investigate which variability modes contain more variance than would be expected if the data were generated by red noise. Our test against red-noise surrogates consisted in 500 Monte Carlo simulations of L independent first-order autoregressive processes at the 95 % significance level. Results of this AR(1) test are plotted in Fig. 4. In this figure, we show the projection of
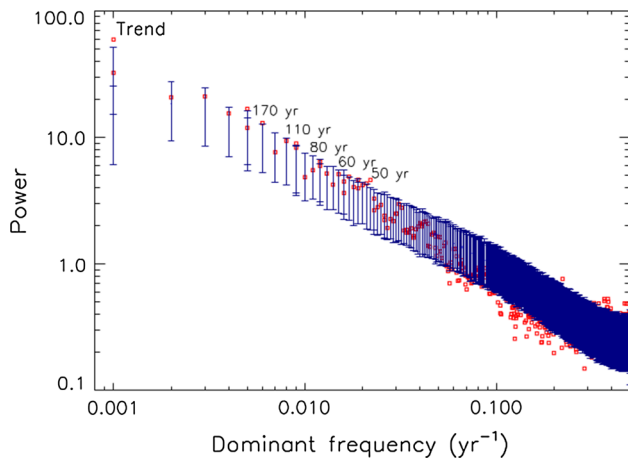
Fig. 4 Monte Carlo significance test of yearly temperature anomaly data in the Northern Hemisphere (NH) for the interval AD 1000–1935, using all $L = 26$ time series available as input channels over this interval. Shown are projections of the temperature data onto the AR(1) null-hypothesis basis, with a 300-year window ($M = 300$). *Open squares* show the data eigenvalues, plotted against the dominant frequency of the corresponding ST-PC; see the "Appendix" for details. The *vertical bars* give the 95 % confidence interval computed from 500 realizations of a noise model consisting of L independent AR(1) processes with the same variance and lag-1 autocorrelation as the input data channels. The dominant periods of the significant components are also indicated. Please see the "Appendix" for technical details

Table 2 Significant components according to the Monte Carlo MSSA test for $L = 26$ channels and $M = 300$ years

ST-PC number	Dominant period (years)	Variance (%)
1–2	Trend	18.5
6–8	170	6.1
9–10	110	3.3
12–13	80	2.1
16–17	50	1.7
18–19	60	1.6

Corresponding variances are also shown

the data onto the red-noise basis associated with the AR(1) null hypothesis; see also Allen and Smith (1996), Ghil et al. (2002) and the "Appendix" here.

High variance appears at both multi-decadal and centennial time scales, relative to what would be expected under the red-noise hypothesis. The significant components are ST-PCs 1–2 (long-term trend), 6–8 (170 years), 9–10 (110 years), 12–13 (80 years), 16–17 (45 years) and 18–19 (60 years). The percentages of variance associated with these modes are reported in Table 2, along with the periods. The combined variance associated with these six modes is of 33.3 %, i.e., exactly one-third of the total.

The MSSA results thus confirm the presence of multi-decadal and centennial oscillations in the data: the periodicities in Table 2 are a representative subset of those captured by SSA and CWT analysis of the single time series, cf. Table 6. As shown in Fig. 5, the two ST-PCs in each of the pairs 9–10, 12–13, 16–17 and 18–19 share a very similar frequency and are in quadrature; these two facts together support the oscillatory nature of the four above modes.

The ST-PC pair 1–2 represents the so-called trend component, whose period, if any, falls outside the window length M. Actually, a millennial oscillation is clearly present in the longest record of the set (Lower Murray Lake, ML), which covers the last 5,000 years; see Table 6. Finally, the ST-PC triplet 6–8, with a dominant period of

roughly 170 years, is statistically significant, although its three PCs behave more irregularly than the pairs. We verified the robustness of all the above results with respect to different values of the window length M by repeating the Monte Carlo test for MSSA with $M = 240$ and 360 years.

A few significant components were also found at periods below 5 years. In particular, oscillatory pairs with periods of about 2.5 and 4.5 years appear to be significant at the 95 % confidence level in Fig. 4. These periods may be associated with the El Niño–Southern Oscillation phenomenon, which is a major source of seasonal-to-interannual climate variability (Jiang et al. 1995 and references therein). In this paper, however, we concentrate on multi-decadal and centennial periodicities, and will not discuss the latter, high-frequency modes any further.

The final step of MSSA was the reconstruction of the space-time series associated with each oscillatory pair by computing the reconstructed components (RCs) associated with it; see the "Appendix" for the corresponding methodological details. The resulting RCs are time series displaying the time evolution of each channel on the time scale of the corresponding MSSA mode.

Figures 6 and 7 represent the evolution in time of temperature anomalies of all the statistically significant RC pairs reconstructed from the MSSA analysis. In the upper half of the panel for each RC pair, this evolution is plotted as a function of increasing latitude (Fig. 6a–f) and by regional group (Fig. 7a–f); the latter groups are listed in Table 3. In the lower half of the corresponding panel we show the RC pair averaged over two different latitude bands (30–60°N and 60–90°N; Fig. 6a–f) and over the eight different regions shown in Fig. 1 (Fig. 7a–f). In all the latter plots, the black solid line represents the average over the whole NH, i.e. the black solid lines in panels Figs. 6a and 7a, etc., are the same.

The trend is well described by the first two MSSA components (RCs 1–2) that represent the most energetic mode, which carries almost one-fifth of the total variance. This millennial oscillation marks the Medieval Warm Period (MWP)—also called the Medieval Climate Anomaly
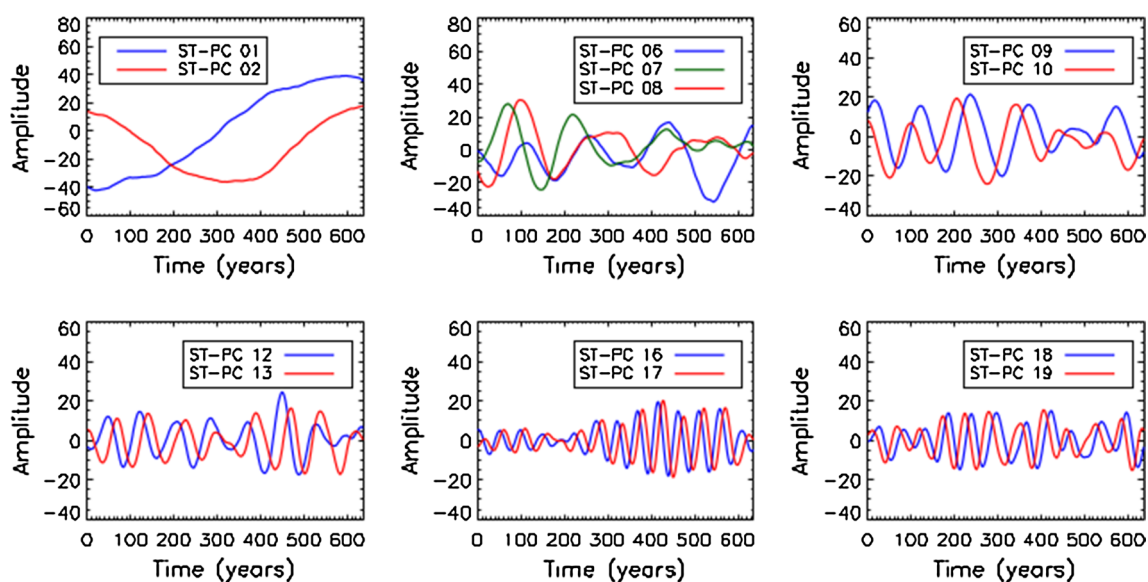
Fig. 5 Time series of MSSA principal component (ST-PC) groups 1–2, 6–8, 9–10, 12–13, 16–17 and 18–19 of yearly NH temperature normalized anomalies; of these six groups, four clearly correspond to oscillatory modes with a period of 110, 80, 50 and 60 years, respec- tively. The MSSA analysis was done for the interval AD 1000–1935, and the 637-year time span on the horizontal axis corresponds to $N' = N - M + 1$; see text for details

(PAGES 2k Consortium 2013)—and the Little Ice Age (LIA) and it is present in both latitude belts under consideration, cf. Fig. 6a.

The corresponding lower half-panel shows that the average NH temperature variation between the MWP and the LIA is of about 0.4 °C, while the temperature difference at mid-latitudes (30–60°N) is somewhat smaller. This is very similar to the amplitude of centennial-scale variability found in most multi-proxy temperature reconstructions for the Northern Hemisphere, e.g., Masson-Delmotte et al. (2013). The upper half-panel clearly indicates that the cooler temperatures associated with the LIA appear first in mid-latitudes and propagate on to higher latitudes. The contributions to the net modern temperature rise come mainly from the trend and from RCs 6–8 (period 170 years; see Table 2).

In Fig. 8 we plot the amplitude pattern for the long-term trend at intervals of 175 years over the last millennium. We notice that the warm conditions related to the MWP are reached at about the same time over the entire NH (see maps corresponding to 1050 and 1225 year AD), and so are the cold conditions that characterize the LIA (see maps corresponding to 1575 and 1750 year AD). Europe and Asia, however, seem to be more prompt in cooling toward LIA (see the map at 1400 year AD) and in recovering after the LIA (see maps at 1750 and 1925 year AD). This fact is clearly confirmed by the Asian (red and purple) curves of Fig. 7a.

Focusing on the centennial oscillation (RCs 9–10), Figure 6c indicates that this mode is present—by-and-large,

except for a few lower-latitude proxies—in the whole data set. Visual inspection yields good phase coherence among all latitudes, with some signal propagation noticeable across latitude belts, over time intervals of the order of a century (*upper half-panel*). A lower amplitude of this oscillation is apparent during the LIA (*lower half-panel*). Conversely, the 50–60-year oscillations (RCs 16–19) are particularly strong in the second half of the last millennium, especially at mid-latitudes.

For the latitude-band-averaged curves in the lower half panels of Fig. 6, visual inspection likewise suggests good phase agreement of the significant modes of variability, at least for the trend and the three leading oscillatory modes; the latter four modes together capture about a third of the total variance of the data set. This consistency is reduced for the last two panels in Fig. 6, as well as when the amplitudes of the oscillations are smaller in its panels (b)–(d); it disappears altogether when grouping the series by longitude (not shown) or by geographical regions. This fact suggests that there are regional differences in the phasing of the NH-wide oscillations.

We investigate these differences in the oscillations' spatio-temporal behavior in the next three figures. Figures 9, 10 and 11 confirm that spatial coherence of temperature variations is quite high, for each significant oscillation. We plot in each of these figures the amplitude pattern at intervals of half a period over three full cycles, for the 170-, 110- and 80-year oscillations, respectively.

All three figures show a great spatial uniformity of temperature over Europe—i.e., to be precise, both the EU1 and

Fig. 6 Latitude dependence of the significant modes of variability, in groups of reconstructed components (RCs): **a** RCs 1–2, **b** RCs 6–8, **c** RCs 9–10, **d** RCs 12–13, **e** RCs 16-17, and **f** RCs 18–19; *color bar* for amplitude $-0.20 - 0.20$ (nondimensional units). *Upper-half panels* RC pairs of temperature anomalies from the MSSA analysis as a function of increasing latitude; *lower-half panels* the same RC pairs averaged over two latitude bands—30–60°N (*orange*), 60–90°N (*green*) and over the entire NH (*black*)
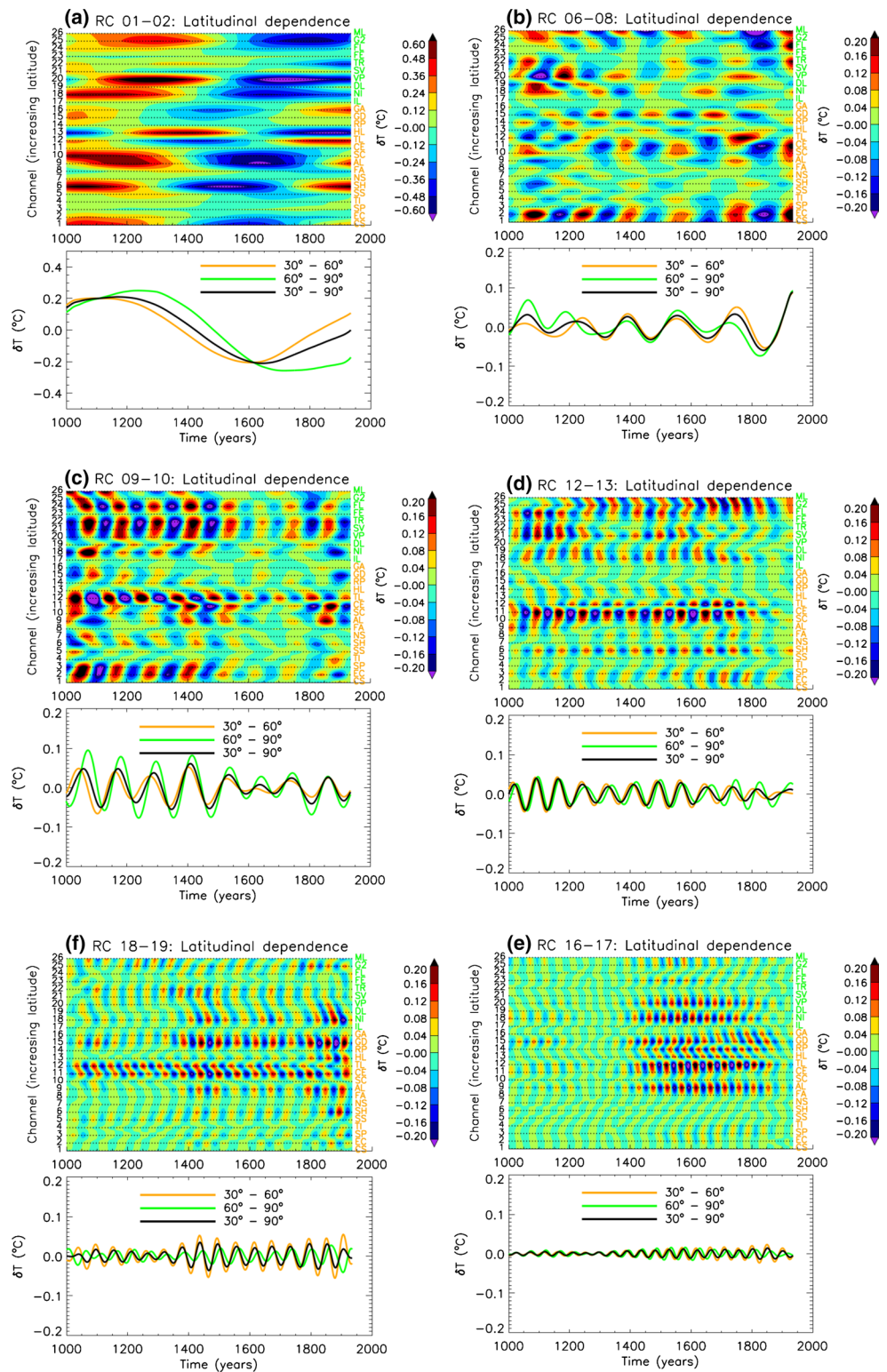
EU2 regions of Fig. 1—with an amplitude of about 0.4 °C. Moreover, the 170-, 110- and 80-year modes in Europe, as well as the 60-year mode (not shown), are in anti-phase with respect to the AR1 region, namely Greenland and the subpolar North Atlantic around Iceland: a warming in EU1

and EU2 corresponds to a cooling in AR1 and vice versa. This behavior is reminiscent of the Greenland–Europe seesaw that is well known to synoptic meteorologists, on shorter time scales, from instrumental data (Loon and Rogers 1978; Kimoto and Ghil 1993).

Fig. 7 Same as Fig. 6, but for regional dependence
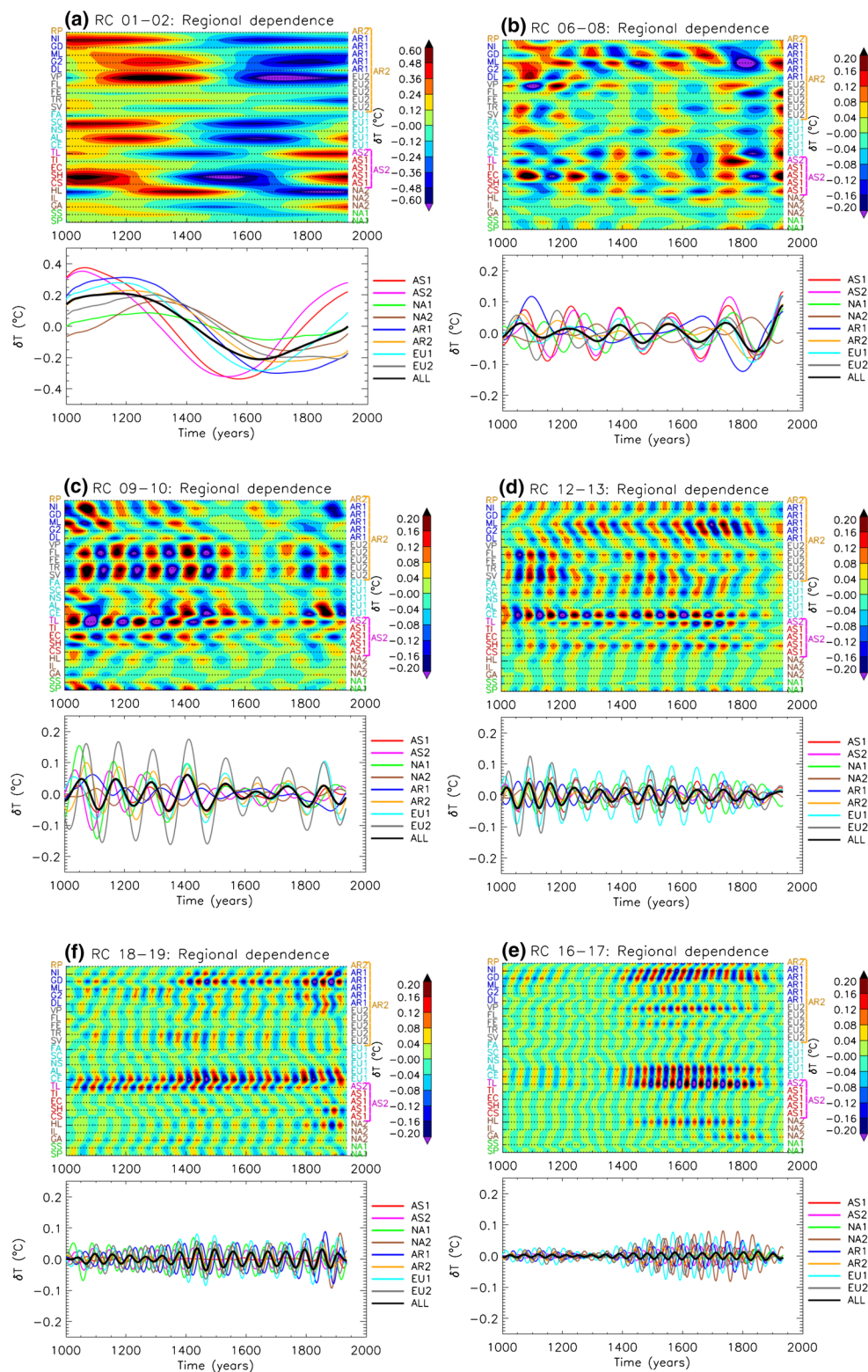
The phase opposition is clear until about AD 1650. Interestingly, Kobashi et al. (2013) identified a similar negative correlation between the reconstructed temperature from Greenland ice-core data since AD 1200, on the one hand, versus the reconstructed interdecadal variability of the rest of the NH and the interdecadal total solar irradiance

Table 3 Regional groups of temperature reconstructions

Group	Time series
AR 1	ML-G2-DL-NI-GD
AR 2	ML-G2-DL-NI-GD-VP-TR-FL-SV-FE-RP
AS 1	TI-SH-EC-CS
AS 2	TI-SH-EC-CS-TL
EU 1	CE-FA-NS-SC-AL
EU 2	VP-TR-FL-SV-FE
NA 1	SS-SP
NA 2	HL-GA-IL

The acronyms stand for *AR* Arctic, *AS* Asia, *EU* Europe, *NA* North America; the regions are outlined on the map in Fig. 1

(TSI), on the other. Larsen et al. (2013) also found that valley glacier fluctuations on Iceland and in the European Alps occurred asynchronously during parts of the Little Ice Age.

With respect to the roughly 0.4 °C peak-to-peak amplitude of the temperature oscillations found in the dataset (Figs. 9, 10, 11), it is important to note that most calibration methods underestimate the amplitude of the trend and the low-frequency variability of the reconstructed temperature changes. According to pseudo-proxy experiments, the underestimates are of the order of 20–50 % (Christiansen et al. 2009 and references therein). We could thus estimate

the actual amplitude of this low-frequency variability over the last millennium to have been of about 0.5 °C or even larger.

4.2 The last millennium: possible causes of variability

Possible causes of climate variability on time scales of decades to centuries include variations in solar activity and ocean circulation. In particular, the oceans play an important role in the climate system because of their large heat capacity and their slow changes in circulation patterns (Ghil 2001; Dijkstra and Ghil 2005). Observational studies (Schlesinger and Ramankutty 1994) and coupled ocean–atmosphere model simulations (Delworth and Mann 2000) suggested a multi-decadal spatio-temporal variability pattern with an amplitude of 0.4 °C in the North Atlantic SST field. This variability pattern has an approximate periodicity of 50–80 year and it is referred to as the Atlantic Multi-decadal Oscillation [AMO; Kerr 2000].

Over the instrumental period, i.e. after about AD 1850, the AMO exhibits approximately two cycles, with warm phases at roughly 1860–1880 and 1930–1960 and cool phases during 1905–1925 and 1970–1990 (Jones et al. 2012). The SST anomaly associated with the AMO covers the entire North Atlantic basin, and its mechanism is linked with northward heat transport variations in the
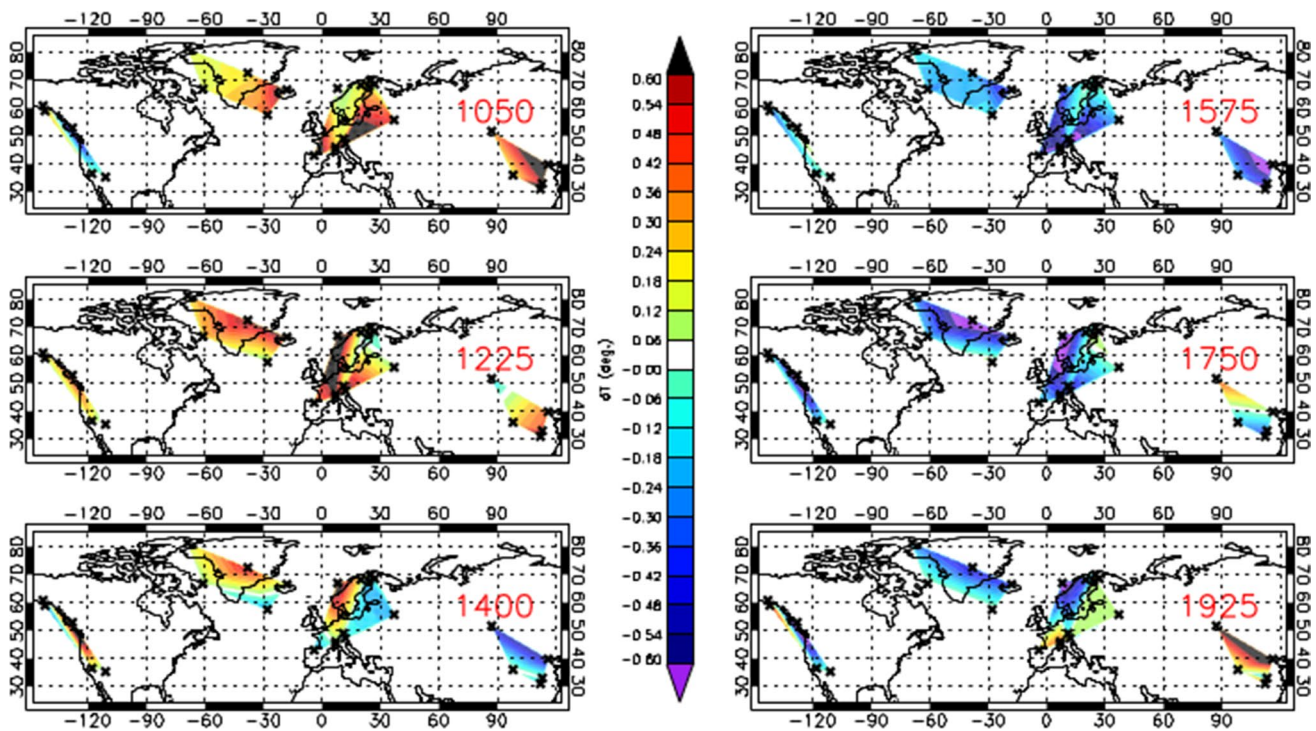

Fig. 8 RC pair 1–2 of temperature anomalies that captures the long-term trend. The spatial patterns are shown at intervals of 175 years, starting from 1050 AD to 1925 AD. The contour interval for the anomalies is 0.06 °C, while the maximum and minimum contours are at ±0.6 °C, respectively

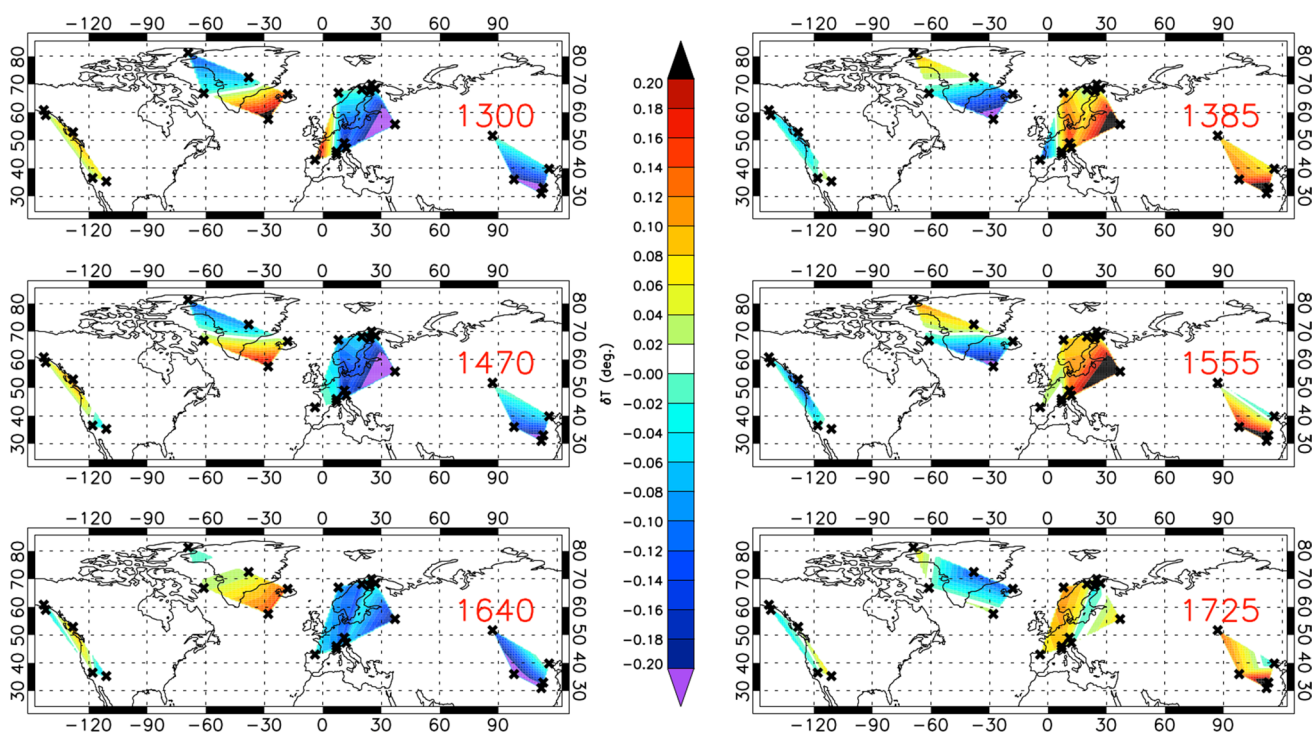**Fig. 9** RC triplet 6–8 of temperature anomalies that captures variability on the time scale of ∼170 years. The spatial patterns are shown at half-period intervals, over three full cycles of the oscillation. The contour interval for the anomalies is 0.02 °C; the maximum/minimum contours are at ±0.2 °C respectively
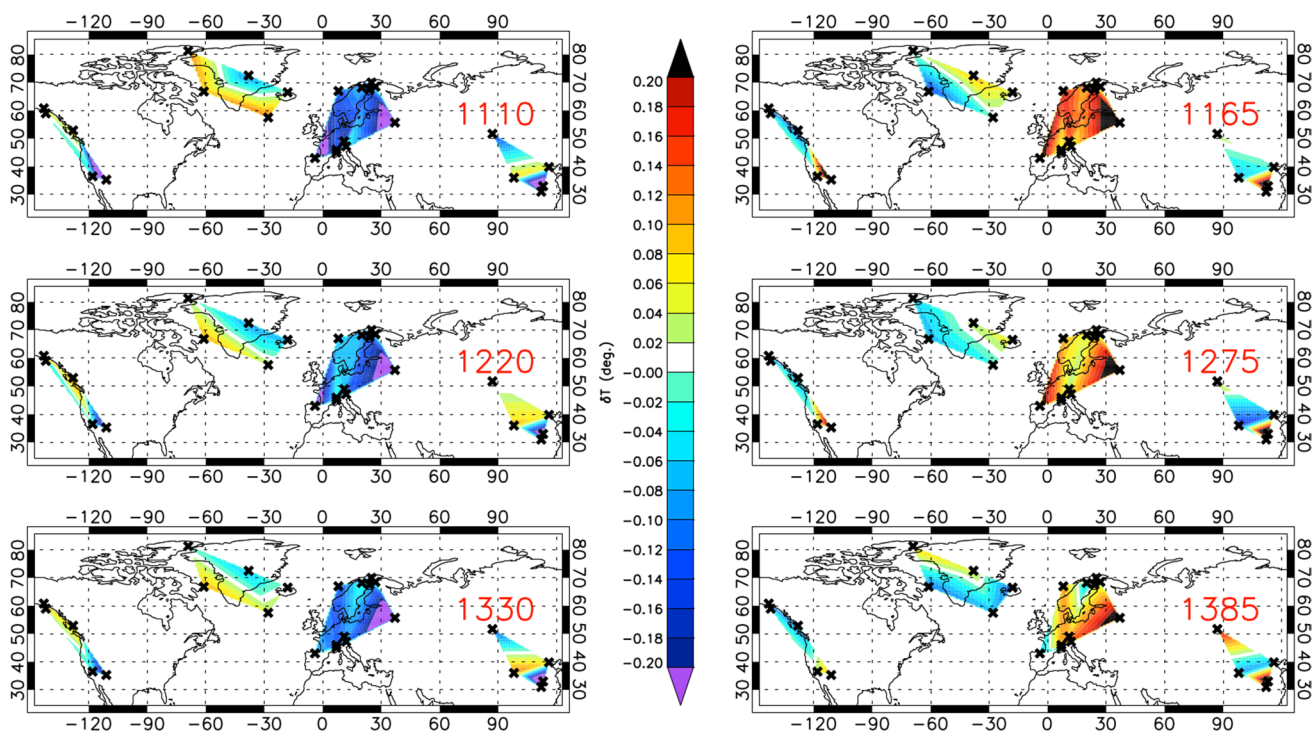

Fig. 10 Same as Fig. 9 but for RC pair 9–10, with its ∼110-year time scale
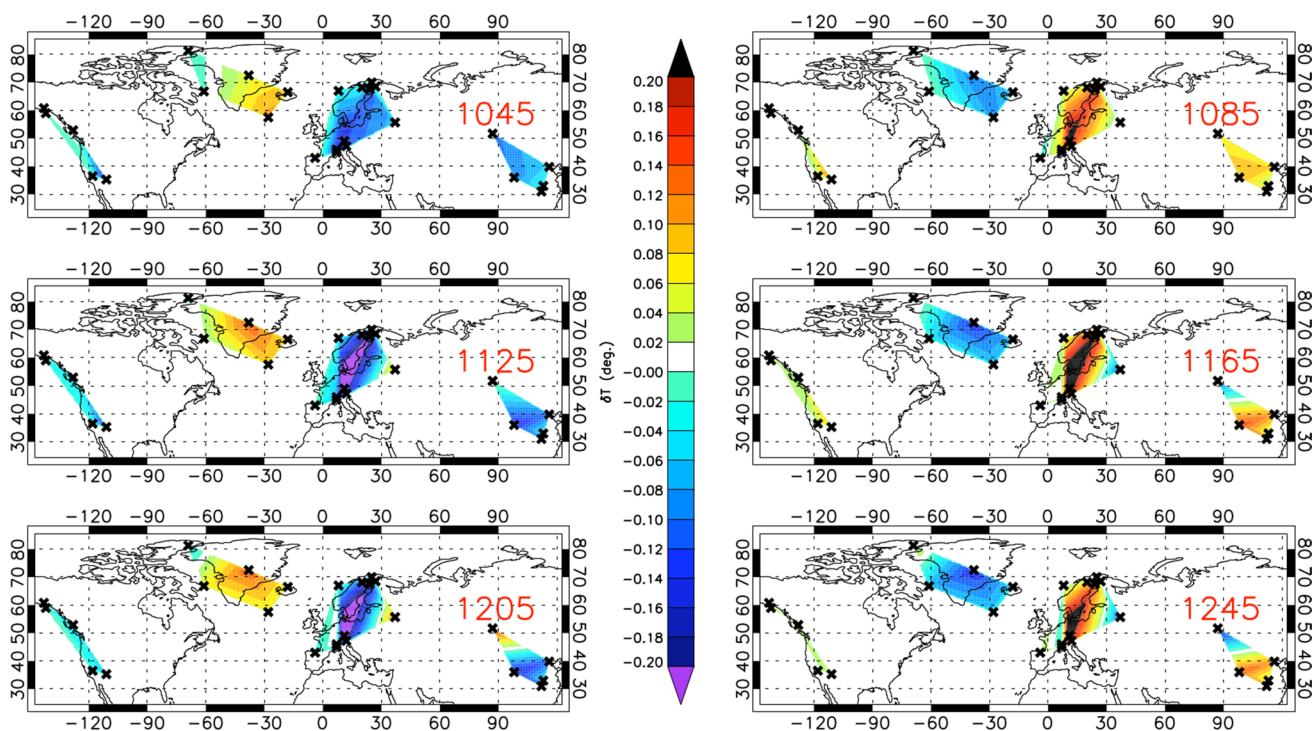
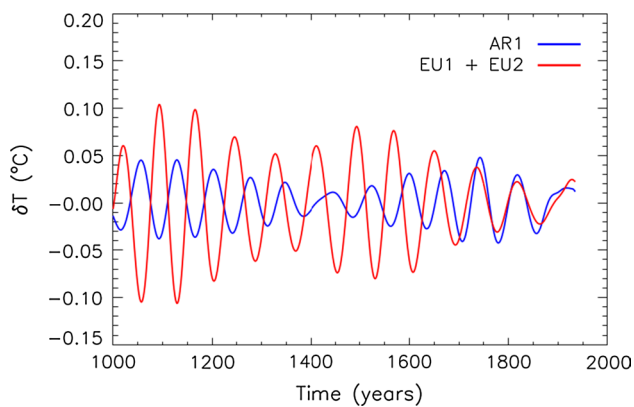**Fig. 11** Same as Fig. 9 but for RC pair 12–13, with its ∼80-year time scale

Fig. 12 Reconstruction of the 80-year oscillations (RCs 12–13) for Europe (EU1+EU2 regions, *red*) and the Greenland+Iceland region (AR1, *blue*)

thermohaline circulation. During its extreme phases, the entire North Atlantic Ocean is dominated by monopolar SST anomalies. The multi-decadal variations in Atlantic SST influence much of the NH climate; they exert, in particular, a significant influence on regional climates as far away as China (Wang et al. 2013).

The results of our analysis, cf. Table 2 and Figs. 7, 11, imply that multi-decadal variability on the time scale of 50–80 years in the North Atlantic may have been active over much of the last millennium. It is difficult, though, to

investigate the detailed relations between the AMO and the multi-decadal climate variability in our proxy records, on the one hand, and the full pattern of surface temperatures over the past millennium, on the other (Mann et al. 2009). More importantly, causal links between either of these reconstructions and the actual mechanism of the AMO over longer times are elusive, due to the lack of reliable proxies for changes in the ocean circulation on these time scales.

The extent to which solar-activity variations affect climate has been a subject of considerable controversy on all time scales (Siscoe 1978; Cubasch et al. 1997; Marcus and Ghil 1999; Velasco and Mendoza 2008; Gray et al. 2010; Lovejoy and Schertzer 2012). Several authors have reported correlations between solar activity—which is reflected in sunspot frequency and in various terrestrial proxies—and climate proxies, hinting that century-scale oscillations in the global mean temperature are linked with similar oscillations in solar activity. Solar-activity proxies are, however, masked by climatic variations and by other climate forcing agents, such as volcanic sulphate aerosols (Breitenmoser et al. 2012).

Among the authors who have claimed solar effects at the centennial scale, Ogurtsov et al. (2013) investigated the cyclicity present in tree-ring records from the Swedish Scandes to the Kola Peninsula and found two oscillatory modes of 55–100 and 100–140 years to be consistent with solar variability at the same time scales. Raspopov et al.

(2008) found approximate 200-year cyclical variations in both the precipitation and temperature signal from juniper tree-ring width data from Central Asia, and related them to the so-called Suess or de Vries solar cycle at roughly 210 years.

Wiles et al. (2004) showed evidence for variations in glacial activity in the mountains of Southern Alaska consistent with the de Vries solar cycle. The Asian monsoon systems also exhibit persistent variability at periodicities corresponding to known solar cycles. Ji et al. (2005) could, using reflectance spectroscopy of a sediment core, show significant periodicities of 123, 163, 200 and 293 years in monsoon moisture over the Qinghai-Tibet Plateau for the past 18,000 years.

The $\delta^{18}O$ and $\delta^{13}C$ speleothem data from Dongge Cave in southern China studied by Dykoski et al. (2005) has shown periodicities of 208, 86 and 11 years in monsoon strength over the last 16,000 years. An analysis by Lim et al. (2005) of a high-resolution sediment record from Korea revealed periodicities of 280, 210 and 137 years in northwesterly winter monsoonal winds over at least the last 6,500 years. Kitagawa and Matsumoto (1995) examined $\delta^{13}C$ variations, which they interpreted as a temperature proxy, in Japanese cedars (*Cryptomeria japonica*) in southern Japan over the last two millennia and found significant temperature periodicities of approximately 187, 89, 70, 55, and 44 years.

In North America, Springer et al. (2008) found periodicities of ~200 and ~500 years of drought in the Sr/Ca ratios and $\delta^{13}C$ data from a West Virginia stalagmite record. A spectral analysis by Yu and Ito (1999) of a 2,100-year–long lake sediment from north-central North Dakota showed dominant periodicities of drought at intervals of about 400, 200, 130 and 100 years. Willard et al. (2005) performed a multi-taper harmonic and power spectral analyses of pollen assemblages from Chesapeake Bay for the past 10,000 years and found highly significant oscillations of about 148, 177, 282, 521 and 1429 years.

Our spectral analysis, based on a multichannel approach rather than a single-series one, allows avoiding this proliferation of spectral peaks and identifies for the NH a significant centennial temperature oscillation. By comparing in Fig. 13 the centennial reconstructed mode (RC 9–10) with the sunspot number series available since ~1700 AD, we cannot fail but notice an apparent agreement with amplitude modulation of the 11-year Schwabe cycle. This visual comparison, however, cannot yield a conclusive answer to the question of whether the two distinct oscillations in the figure are actually connected, due to the short time interval available. It is also important to keep in mind that state-of-the-art reconstructions of TSI over the Holocene (Steinhilber et al. 2012) do not find the Gleissberg cycle nor the de Vries cycle or other periodicities in solar variability to be highly significant.
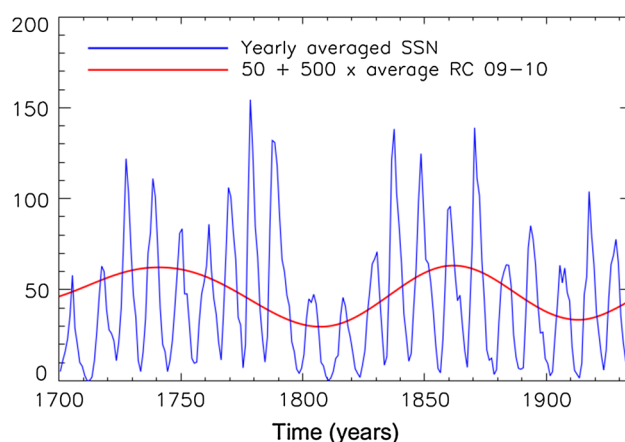
Fig. 13 Comparison between the sunspot number series (*blue*) and the reconstructed centennial mode (RCs 9–10, *red*). For presentation purposes, the centennial mode is shifted and multiplied by an arbitrary factor
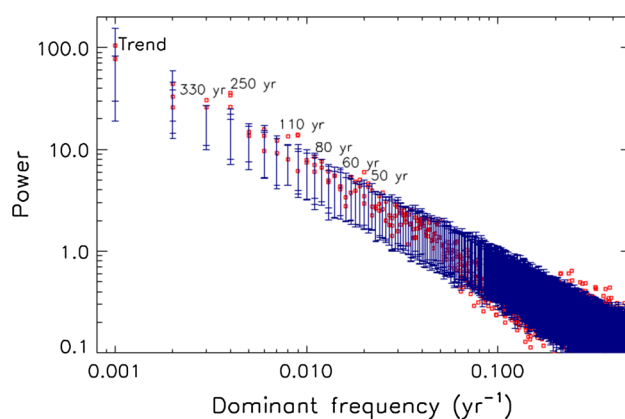
Fig. 14 Same as Fig. 4, except for the time interval 116–1935 AD, $L = 17$ time series, $M = 600$ years, and 200 surrogate time series

4.3 The last two millennia

In order to exploit the fact that several proxy records are much longer than 1,000 years and to confirm our previous results, we further applied the MSSA methodology to a reduced data set for the common 1820-year interval spanning 116 to 1935 AD, i.e. $N = 1,820$. In this way, we obtained a data set with $L = 17$ series.

In this case, we used a window width of $M = 600$ years and applied the Monte Carlo–MSSA test of Allen and Robertson (1996) to this subset of proxy records. The test consisted in 200 Monte Carlo simulations of L independent first-order autoregressive processes AR(1) at the 95 % significance level, and its results are illustrated in Fig. 14. In this figure, we show the projection of the data onto the red-noise null-hypothesis basis.

High variance appears at both multi-decadal and centennial time-scales, relative to what would be expected under

Table 4 Significant components identified by Monte Carlo-MSSA for $L = 17$ channels and $M = 600$ years

ST-PC number	Signif. period (year)	Variance (%)
1–2	Trend	18.8
10–12	330	4.6
3–5	250	10.2
13–14	110	2.7
23–24	80	1.3
31–32	60	1.0
37–38	50	0.8

the red-noise assumption. The significant components are the trend (RCs 1–2), RCs 10–12 (330 years), RCs 3–5 (250 years), RCs 13–14 (110 years), RCs 23–24 (80 years), RCs 31–32 (60 years) and RCs 37–38 (50 years). The percentages of variance associated with these modes are reported in the last column of Table 4, and they represent a total of almost 40 %, versus only 33 % in Table 2.

Table 4 and Fig. 14 here extend to the last two millennia the results obtained in Sect. 4.1 for the last millennium. The greater window width, $M = 600$ years here versus $M = 300$ years there, allows for greater spectral resolution and also for the presence of a greater number of components that just capture the continuous spectral background between the peaks. Still, the peaks at 50, 60, 80 and 110 years appear as significant in both analyses—although the order of the peaks at 50 and 60 years is inverted with respect to Table 2, and the 80-year mode is only significant at 90 % here, as is the trend. Recall, though, that in both the millennial and bimillennial analysis, the ratio N/M is barely higher than three, thus limiting the statistical significance (Vautard and Ghil 1989; Ghil et al. 2002).

The greater M and N also allow one to divide the lowest frequencies into three, rather than only two significant modes: trend, 330 and 250 years here vs. trend and 170 years in the millennial analysis. Clearly, any mode whose time scale exceeds 300 years would be absorbed into the trend in Table 2, while a mode with period 250 years, i.e. approaching 300 years, could be aliased into the 170 years mode there. The better spectral resolution, though, comes at the cost of lower spatial resolution: clearly 17 records provide less of a basis for analyzing regional behavior than 26.

5 Concluding remarks

The purpose of this study was to perform multi-spectral analysis to describe the spatio-temporal variability of near-surface air temperatures over the Northern Hemisphere (NH), based on a fairly large set of calibrated proxy records

(see Figs. 1, 2; Table 5), with an emphasis on variability at multi-decadal and centennial time scales.

Our approach differs from previous spectral analyses of paleoclimatic data in its choice of analyzing only high-resolution proxy records that were calibrated to temperature by their original authors. This choice allows one to preserve the optimal information about temperature variations at each geographic location.

Using three distinct, single- and multivariate spectral approaches (see the "Appendix"), we found persistent and highly significant multi-decadal and centennial temperature variations in our NH data set (see Figs. 3, 4, 5, 14; Table 2, 4), with distinct spatial features displaying major areas of variability. Variability on longer time-scales is carried by a dominant trend component, whose spatio-temporal features are consistent with both the Medieval Warm Period (MWP) and the Little Ice Age (LIA). These features extend over the entire NH, with Europe and Asia somewhat ahead of the rest of the hemisphere; see Fig. 8.

The spatio-temporal structure of the oscillations has been characterized using latitudinal and regional groupings of the reconstructed components (RCs). Grouping the proxy records by latitude bands (Fig. 6), we found good phase agreement among the significant oscillations in the same latitude band, at least for the trend and the secular components. Phase propagation from mid to high latitudes is observed in certain cases, especially for the trend (RCs 1-2, Fig. 6a) during the LIA, with a characteristic travel time of one-to-two centuries.

The grouping by geographical regions (Table 3; Fig. 7) also provides visual evidence of signal propagation from one region to another, in particular on the centennial time scale (Fig. 7c, d). In fact, spatial maps reconstructed for each mode (Figs. 9, 10, 11) strongly suggest that the centennial and the multi-decadal oscillations in Europe and in part of the Arctic region are in anti-phase, with a warming in Europe corresponding to a cooling in the Arctic and vice versa (see Fig. 12).

Although the same oscillations are present in all the geographical regions that are represented in our data set, their spectral power differs. In particular, the North American proxies (regions NA1 and NA2) exhibit a reduced amplitude at all time scales over the last millennium (see lower panels of Fig. 7) with respect to the other regions. This is in line with the results of Shabalova and Weber (1999), who also found the amplitude of multi-decadal temperature oscillations to be larger in Europe than in North America and even absent altogether in northwestern North America. The 110-year oscillation is particularly strong over Northern Europe (EU2 region), especially the first half of the last millennium (Fig. 7c, lower panel).

Finally, the results in Fig. 13 suggest a possible link of the secular temperature variations reflected in our proxies

with solar forcing, and in particular with the Gleissberg and the de Vries cycles that modulate the 11-year cycle.

Appendix 1: Singular Spectrum Analysis (SSA)

The SSA methodology involves three basic steps: (1) embedding a time series of length N in a vector space of dimension M—for the choice of M, see Vautard et al. (1992) and Ghil et al. (2002; 2) computing the $M \times M$ lag-covariance matrix C_D of the data—see the two different approaches of Broomhead and King (1986) and Vautard and Ghil (1989); and (3) diagonalizing C_D:

$$\Lambda_D = E_D^T C_D E_D, \tag{2}$$

where $\Lambda_D = \mathrm{diag}(\lambda_1, \lambda_2, \ldots \lambda_M)$, with $\lambda_1, \lambda_2, \ldots \lambda_M > 0$ the real, positive eigenvalues of the symmetric matrix C_D, and E_D is the $M \times M$ matrix having the corresponding eigenvectors $\mathbf{E_k}, k = 1, \ldots M$, as its columns.

For each $\mathbf{E_k}$ we construct the time series of length $N - M + 1$, called the k-th principal component (PC); this PC represents the projection of the original time series on the eigenvector $\mathbf{E_k}$, also called empirical orthogonal function (EOF). Each eigenvalue λ_k gives the variance of the corresponding PC; its square root is called a singular value.

Given a subset $\mathcal{K} = (k_1^*, k_2^*, \ldots k_K^*)$ of eigenvalues, it is possible to extract time series of length N, by combining the corresponding PCs. These time series are called reconstructed components (RCs) and capture the variability associated with the K eigenvalues of interest. A nonlinear, data-adaptive trend is typically identified by the largest eigenvalue and the associated EOF that has no zero. An oscillatory mode is associated with a pair of nearly equal eigenvalues, while the corresponding EOFs are in quadrature, like a pair of anharmonic, data-adaptive sine and cosine.

In order to reliably identify the trend and oscillations in a series, the Monte Carlo method (MCSSA) is used (Allen and Smith 1996). In this approach, one assumes a model for the analyzed time series and one determines this model's parameters using a maximum-likelihood criterion; one refers to this model commonly as the null hypothesis.

Then a Monte Carlo ensemble of surrogate time series is generated from the null hypothesis, and SSA is applied to the data as well as the surrogates, in order to test whether it is possible to distinguish the original time series from the ensemble of surrogates. Since a large class of geophysical

processes generate series with larger power at lower frequencies (Ghil et al. 2002), we assume AR(1) noise in evaluating evidence for trend and oscillations. This is done to avoid overestimating the significance of the low-frequency peaks in the spectrum, by underestimating the amplitude of the stochastic component of the time series in the lower part of the frequency range (Allen and Smith 1996; Ghil et al. 2002).

Appendix 2: Multichannel SSA (MSSA)

In order to reconcile the different information items contained in each of the data sets under study, it is useful to apply the SSA analysis to a combination of all the available measurements, and not just to each one separately. Doing so may allow us to extract a subset of oscillations that are common to all the time series, thus establishing which periodicities are the most dominant for the whole data set.

Multichannel Singular Spectrum Analysis [MSSA; Keppenne and Ghil (1993); Plaut and Vautard (1994)] is a multivariate extension of the SSA method, with each *channel* corresponding to one of the time series of interest. As in the univariate case, this data-adaptive filtering technique can identify nearly periodical oscillating modes within a specified spectral window. This method is equivalent, in principle, to extended empirical orthogonal function analysis [EEOF: Weare and Nasstrom (1982)], but in MSSA the focus is on the temporal structure of the variability, whereas in EEOF it is the spatial variability that is emphasized.

Basically, MSSA decomposes a multichannel time series $\mathbf{X}_{l,i}$, with $i = 1, \ldots, N$ representing time and $l = 1, \ldots, L$ the channel number, into an orthonormal, data-adaptive space-time structure whose elements represent eigenvectors grand cross-covariance matrix of size $LM \times LM$, where M is the window width. The computation thus results in a set of eigenvectors $\mathbf{E}^k$, called space-time EOFs (ST-EOFs), and their associated space-time PCs (ST-PCs) a^k, computed by projecting $\mathbf{X}$ onto $\mathbf{E}^k$. The $L \times M$ real eigenvalues λ_k, each associated with the k-th eigenvector $\mathbf{E}^k$, equal the variance in the a^k direction.

The MSSA expansion of the original data series is thus given by

$$\mathbf{X}_{l,i+j} = \sum_{k=1}^{LM} a_i^k \mathbf{E}_{ij}^k, \quad i = 1, \ldots, N; \quad j = 1, \ldots, M. \tag{3}$$

Each reconstructed component (RC) allows one to reconstruct the dynamical behavior in $\mathbf{X}$ that belongs to $\mathbf{E}^k$ (Plaut and Vautard 1994; Ghil et al. 2002).

Table 5 Characteristics of the 26 temperature time series in our data set

Acronym	Name	Long.	Lat.	Archive	Proxy type	Season	Time span (year)	Δt (year)	N	References
ML	Lower Murray Lake	−69.32	81.21	LS	Mass accumul. rate	July	3236 BC–1969 AD	1	5,206	Cook et al. (2009)
G2	GISP2	−38.5	72.6	IC	$\delta^{15}N$ and $\delta^{40}Ar$	Annual	2000 BC–1993 AD	1	3,994	Kobashi et al. (2011)
FL	Finnish Lapland	25	69	TR	Ring width	June–Aug	2000 BC–2005 AD	1	4,006	Helama and Macias Fauria (2010)
FE	Fennoscandia (Laanila)	27.3	68.5	TR	Height increment	June–Aug	745 AD–2007 AD	1	1,263	Lindholm et al. (2011)
TR	Torneträsk	19.80	68.31	TR	Density	Apr–Aug	500 AD–2004 AD	1	1,505	Grudd (2008)
SV	Northern Scandinavia	25	68	TR	Density	June–Aug	138 BC–2006 AD	1	2,145	Esper et al. (2012)
VP	Vøring Plateau	7.64	66.97	MS	Foraminifer	Summer	883 BC–1995 AD	Irregular	281	Andersson et al. (2010)
DL	Donard Lake	−61.35	66.66	LS	Varve thickness	June–Aug	752 AD–1992 AD	1	1,241	Moore et al. (2001)
NI	North Icelandic Shelf (MD99-2275)	−19.3	66.3	MS	$U_K^{37'}$ Alkenone	July	2549 BC–1997 AD	Irregular	1,029	Sicre et al. (2011)
IL	Iceberg Lake	−142.95	60.78	LS	Varve thickness	May–June	442 AD–1998 AD	1	1,557	Loso (2009)
GA	Gulf of Alaska	−145	60	TR	Ring width	Jan–Sept	724 AD–2002 AD	1	1,279	Wilson et al. (2007)
GD	Gardar Drift (RAPiD21-3K)	−27.91	57.45	MS	$U_K^{37'}$ Alkenone	Summer	5 BC–1959 AD	Irregular	269	Sicre et al. (2011)
RP	Russian Plains	45	45	MP	–	Annual	5 AD–1995 AD	10	199	Sleptsov and Klimenko (2003)
HL	Hallet Lake	−146.2	61.5	LS	Biogenic silica	June–Aug	116 AD–2000 AD	Irregular	174	McKay et al. (2008)
TL	Teletskoe Lake	87.61	51.76	LS	Biogenic silica	Annual	1018 BC–2002 AD	1	3,021	Kalugin et al. (2009)
CE	Central Europe (Alpine arc)	8	46	TR	Ring width	June–Aug	499 BC–2003 AD	1	2,503	Büntgen et al. (2011)
SC	Spannagel Cave	11.40	47.05	ST	$\delta^{18}O$	Annual	90 BC–1932 AD	Irregular	717	Mangini et al. (2005)
AL	The Alps (Lötschental)	8.0	46.3	TR	Density	June–Sept	499 BC–2003 AD	1	1,250	Büntgen et al. (2006)
FA	French Alps	9	46	TR	Ring width	June–Aug	751 AD–2008 AD	1	1,258	Corona et al. (2011)
NS	Northern Spain	−3.5	42.9	ST	$\delta^{13}C$	Annual	1949 BC–1998 AD	Irregular	875	Martín-Chivelet et al. (2011)
SH	ShiHua Cave	115.56	39.47	ST	Layer thickness	May–Aug	665 BC–1985 AD	1	2,651	Tan et al. (2003)
SS	Southern Sierra Nevada	−118.9	36.9	TR	Ring width	June–Aug	800 AD–1988 AD	1	1,189	Graumlich (1993)
TI	Tibet	98.5	36.5	TR	Ring width	Annual	1000 AD–2000 AD	1	1,001	Liu et al. (2009)
SP	Southern Colorado Plateau	−111.4	35.2	TR	Ring width	June–Aug	250 BC–1996 AD	1	2,247	Salzer and Kipfmueller (2005)
EC	East China	114	35	DO	Historical	Oct–Apr	15 AD–1977 AD	Irregular	116	Ge et al. (2003)
CS	China Stack	100	35	MP	–	Annual	0 AD–1990 AD	10	199	Yang et al. (2002)

The columns in the table give: a two-letter acronym; a full name based on the location (see Fig. 1); longitude and latitude; archive from which the series was extracted and proxy type; season which a given temperature series is referred to; the time span (from t_1 to t_N); the sampling interval Δt; the number of points N; and the published reference

The identification of the archives uses the following abbreviations: *LS* lake sediments, *IC* ice core, *TR* tree rings, *MS* marine sediments, *MP* multi-proxy composite, *ST* speleothems, *DO* documentary

Table 6 Periodicities found by SSA and CWT

Site	~10 years	~20–30 years	~40–70 years	~100 years	~200 years	~300 years	~400 years	~500–700 years	Millennial
ML		*20 years*	*70 years*	*120 years*	**150 years** **220 years**	360 years		**600 years**	**X**
G2				90 years 120 years	190 years	340 years			X
FL		*30 years*	*50 years* *70 years*	*80 years* **90 years** **130 years**	**240 years**	*300 years*	*450 years*	*700 years*	X
FE	**11 years**	**20 years** **30 years**	*50 years*						
TR			70 years	**110 years**	*200 years*	**340 years**		**600 years**	**X**
SV	*11 years*		*50 years*	**80 years** **120 years**			460 years (95 %)		**X**
VP		*20 years (90 %)* *30 years (90 %)*	**40 years**						**X (90 %)**
DL			**70 years**	128 years	**210 years**	300 years (95 %)			**X**
NI	*8.5 years* *11 years (90 %)*	*20 years*							**X**
IL	**11 years**		**70 years**	**110 years**	**220 years**				**X**
GA	**11 years**	**20 years**	*50 years*			320 years (90 %)		490 years (95 %)	**X**
GD		*20 years*	**50 years**			**280 years**		770 years (95 %)	X
RP		*20 years (90 %)*	**50 years**		**250 years**				X
HL			50 years	*100 years (90 %)*		300 years (90 %)			**X (90 %)**
TL				*100 years (90 %)*	*200 years*	*300 years*			**X**
CE			70 years (90 %)	**110 years**	**180 years**			620 years (95 %)	**X**
SC		**20 years (95 %)**						770 years (90 %)	**X**
AL					*200 years*	300 years		670 years	**X**
FA				**90 years**		270 years (90 %)		670 years	**X**
NS		*20 years*							**X**
SH						350 years			**X**
SS	**11 years**								**X**
TI				*80 years* **120 years**	**200 years**				**X**
SP			40 years (95 %) 50 years (95 %) *50 years*	**100 years**	*200 years*				
EC			40 years (90 %)	*100 years (90 %)*	**170 years (90 %)**				X
CS				**100 years (90 %)**	*200 years (90 %)*				**X (90 %)**

The corresponding confidence levels are shown in parentheses only if lower than 99 %).

Values in Bold: periodicities detected by both methods; values in italic: periodicities detected by SSA only; values in roman: periodicities detected by CWT only. In the last column, the symbol X represents the presence of a significant millennial long-term trend

MSSA shares with single-channel SSA the ability to identify robust modulated oscillations in the data with period smaller than M by means of pairs of subsequent eigenvectors that are in phase quadrature, that is, such that the cross-correlation between these pairs is maximum at a lag of roughly one quarter the associated period. In order to select an oscillatory mode, it is required that the corresponding eigenvalues are nearly equal and that the two ST-PCs share aprroximately the same frequency (Vautard et al. 1992; Plaut and Vautard 1994).

As in the case of single-channel SSA, the presence of an eigenvalue pair is not sufficient to conclude that they represent an oscillation in the data. The significance of such tentatively identified oscillations has to be additionally checked, because also pure white- or red-noise processes are able to randomly generate pairs of eigenvectors satisfying the above-mentioned criteria (Vautard and Ghil 1989; Vautard et al. 1992; Allen and Smith 1996).

Allen and Robertson (1996) suggested two different significance tests for the presence of oscillations at low signal-to-noise ratios in multivariate data, based on the same null hypothesis. In the first test, the lag-covariance matrix is computed from the original, observed data, whereas in the second, the lag-covariance matrix is computed from the surrogate data generated by Monte Carlo methods. The subsequent procedure of projecting the data and the noise surrogates onto the ST-EOF basis is similar in both tests. The second test is more robust, since the former implicitly assumes the existence of a signal before any signal has been detected (Allen and Smith 1996).

We have applied both of these tests to determine whether the modes associated with pairs of eigenvalues correspond to actual oscillatory modes. The following step, given the detection of frequencies with significantly more power than expected from red noise, is to reconstruct the multivariate structure associated with each of them. Variability on time scales longer than M is described by the nonlinear, data-adaptive trend component, which however may also represent an oscillation with a time scale larger than M (Ghil and Vautard 1991; Ghil et al. 2002).

Appendix 3: Continuous Wavelet Transform (CWT)

The Wavelet Transform (WT) allows an evolutionary spectral analysis of a series in the time-scale plan (Foufoula-Georgiou and Kumar 1994; Percival and Walden 2000). The concept of scale is typical of this method: the scale is a time duration that can be properly translated into a Fourier period, and hence a frequency. The Continuous Wavelet Transform (CWT) in spectral applications is discretized by computing it at all available time steps and on a dense set of scales (Torrence and Compo 1998).

The square modulus of the transform expresses spectral density as a function of time and frequency. A filtered version of the signal can then be reconstructed selecting only the contributions from a given set of periods. By time averaging the CWT at each value of the period (scale), the Global Wavelet Spectrum (gws)—and the corresponding significance levels, using a background spectrum of red noise—can be computed, thus obtaining a time-averaged spectral estimate comparable with those obtained by classical methods. However, CWT is a multiresolution analysis: frequency resolution is high at low frequencies and poor at high frequencies (Torrence and Compo 1998). It is, therefore, particularly suited for determining the frequency of the oscillations and to reconstruct them accurately in the low-frequency range of the spectrum (Tables 5, 6).

References

Allen MR, Robertson AW (1996) Distinguishing modulated oscillations from coloured noise in multivariate data sets. Clim Dyn 12:775–784

Allen MR, Smith LA (1996) Monte Carlo SSA: Detecting irregular oscillations in the presence of coloured noise. J Clim 9:3373–3404

Alley RB (2000) The Younger Dryas cold intervals as viewed from central Greenland. Quat Sci Rev 19:213–226

Andersson C, Pausata FSR, Jansen E, Risebrobakken B, Telford RJ (2010) Holocene trends in the foraminifer record from the Norwegian Sea and the North Atlantic Ocean. Clim Past 6:179–193

Breitenmoser P, Beer J, Brönnimann S, Frank D, Steinhilber F, Wanner H (2012) Solar and volcanic fingerprints in tree-ring chronologies over the past 2000 years. Palaeogeogr Palaeoclimatol Palaeoecol 313–314:127–139

Briffa KR, Osborn TJ, Schweingruber FH, Jones PD, Shiyatov SG, Vaganov EA (2002) Tree-ring width and density around the Northern Hemisphere: Part 1, local and regional climate signals. Holocene 12:737–775

Broomhead DS, King GP (1986) Extracting qualitative dynamics from experimental data. Phys D 20:217–236

Büntgen U, Frank DC, Nievergelt D, Esper J (2006) Summer temperature variations in the European Alps, A.D. 755–2004. J Clim 19:5606–5623

Büntgen U, Tegel W, Nicolussi K, McCormick M, Frank D, Trouet V, Kaplan JO, Herzig F, Heussner KU, Wanner H, Luterbacher J, Esper J (2011) 2500 years of European climate variability and human susceptibility. Science 331:578–582

Christiansen B, Schmith T, Thejll P (2009) A surrogate ensemble study of climate reconstruction methods: stochasticity and robustness. J Clim 22:951–976

Cook ER, Briffa KR, Meko DM, Graybill DA, Funkhouser G (1995) The 'segment length curse' in long tree-ring chronology development for palaeoclimatic studies. Holocene 5:229–237

Cook TL, Bradley RS, Stoner JS, Francus P (2009) Five thousand years of sediment transfer in a High Arctic watershed recorded in annually laminated sediments from Lower Murray Lake. Ellesmere Island, Nunavut, Canada. J Paleolimnol 41:77–94

Corona C, Edouard JL, Guibal F, Guiot J, Bernard S, Thomas A, Denelle N (2011) Long-term summer (AD 751–2008) temperature fluctuation in the French Alps based on tree-ring data. Boreas 40:351–366

Cronin TM, Hayo K, Thunell RC, Dwyer GS, Saenger C, Willard DA (2010) The Medieval Climate Anomaly and Little Ice Age in Chesapeake Bay and the North Atlantic Ocean. Palaeogeogr Palaeoclimatol Palaeoecol 297:299–310

Cubasch U, Voss R, Hegerl GC, Wazskewitz J, Crowley TJ (1997) Simulation of the influence of solar radiation variations on the global climate with an ocean-atmosphere general circulation model. Clim Dyn 13:757–767

D'Arrigo R, Jacoby G, Frank D, Pederson N, Cook E, Buckley B, Nachin B, Mijiddorj R, Dugarjav C (2001) 1738 years of Mongolian temperature variability inferred from tree-ring width chronology of Siberian pine. Geophys Res Lett 28: doi:10.1029/2000GL011845

Delworth TL, Mann ME (2000) Observed and simulated multidecadal variability in the Northern Hemisphere. Clim Dyn 16:661–676

Dijkstra HA, Ghil M (2005) Low-frequency variability of the large-scale ocean circulation: A dynamical systems approach. Rev Geophys 43:RG3002. doi:10.1029/2002RG000122

Dykoski CA, Edwards RL, Cheng H, Yuan D, Cai Y, Zhang M, Lin Y, Qing J, An Z, Revenaugh J (2005) A high-resolution, absolute-dated Holocene and deglacial Asian monsoon record from Dongge Cave, China. Earth Planet Sci Lett 233:71–86

Enfield Mestas-Nuñez AM, Trimble PJ (2001) The Atlantic multidecadal oscillation and its relation to rainfall and river flows in the continental US. Geophys Res Lett 28:2077–2080

Esper J, Frank DC, Timonen M, Zorita E, Wilson RJS, Luterbacher J, Holzkämper S, Fischer N, Wagner S, Nievergelt D, Verstege A, Büntgen U (2012) Orbital forcing of tree-ring data. Nat Clim Chang 2:862–866

Fernández-Donado L, González-Rouco JF, Raible CC, Ammann CM, Barriopedro David, García-Bustamante Elena, Jungclaus JH, Lorenz SJ, Luterbacher J, Phipps SJ, Servonnat J, Swingedouw D, Tett SFB, Wagner S, Yiou P, Zorita E (2013) Large-scale temperature response to external forcing in simulations and reconstructions of the last millennium. Clim Past 9:393–421

Foufoula-Georgiou E, Kumar P (eds) (1994) Wavelets in geophysics. Academic Press, New York

Franke J, Frank D, Raible CC, Esper J, Brönnimann S (2013) Spectral biases in tree-ring climate proxies. Nat Clim Chang 3:360–364

Ge Q, Zheng J, Fang X, Man Z, Zhang X, Zhang P, Wang WC (2003) Winter half-year temperature reconstruction for the middle and lower reaches of the Yellow River and Yangtze River, China, during the past 2000 years. Holocene 13:933–940

Ghil M (2001) Hilbert problems for the geosciences in the 21st century. Nonlin Process Geophys 8:211–222

Ghil M, Vautard R (1991) Interdecadal oscillations and the warming trend in global temperature time series. Nature 350:324–327

Ghil M, Allen MR, Dettinger MD, Ide K, Kondrashov D, Mann ME, Robertson AW, Saunders A, Tian Y, Varadi F, Yiou P (2002) Advanced spectral methods for climatic time series. Rev Geophys 40:3.1–3.41

Ghil M, Zaliapin I, Thompson S (2008) A delay differential model of ENSO variability: parametric instability and the distribution of extremes. Nonlin Process Geophys 15:417–433

Gildor H, Ghil M (2002) Phase relations between climate proxy records: The effect of seasonal precipitation changes. Geophys Res Lett 29:11.1–11.4 (GL013781)

Graumlich LJ (1993) A 1000-yr record of temperature and precipitation in the Sierra Nevada. Quat Res 39:249–255

Gray LJ, Beer J, Geller M, Haigh JD, Lockwood M, Matthes K, Cubasch U, Fleitmann D, Harrison G, Hood L, Luterbacher J, Meehl GA, Shindell D, van Geel B, White W (2010) Solar influences on climate. Rev Geophy 48:RG4001. doi:10.1029/2009RG000282

Grudd H (2008) Torneträsk tree-ring width and density AD 500–2004: a test of climatic sensitivity and a new 1500-year reconstruction of North Fennoscandian summers. Clim Dyn 31:843–857

Helama S, Macias Fauria M, Mielikäinen K, Timonen M, Eronen M (2010) Sub-Milankovitch solar forcing of past climates: mid and late Holocene perspectives. Geol Soc Am Bull 122:1981–1988

Hocke K, Kämpfer N (2009) Gap filling and noise reduction of unevenly sampled data by means of the Lomb-Scargle periodogram. Atmos Chem Phys 9(12):4197–4206

Horne JH, Baliunas SL (1986) A prescription for period analysis of unevenly sampled time series. Astrophys J 302:757–763

Humlum O, Solheim J-K, Stordahl K (2011) Identifying natural contributions to late Holocene climate change. Glob Planet Change 79:145–156

Ji JF, Shen J, Balsam W, Chen J, Liu LW, Liu XQ (2005) Asian monsoon oscillations in the northeastern Qinghai-Tibet Plateau since the late glacial as interpreted from visible reflectance of Qinghai Lake sediments. Earth Planet Sci Lett 233:61–70

Jiang H, Eiríksson J, Schulz M, Knudsen K-L, Seidenkrantz M-S (2005) Evidence for solar forcing of sea-surface temperature on the North Icelandic Shelf during the late Holocene. Geology 33:73–76

Jiang N, Neelin JD, Ghil M (1995) Quasi-quadrennial and quasi-biennial variability in the equatorial Pacific. Clim Dyn 12:101–112

Jones PD, Lister DH, Osborn TJ, Harpham C, Salmon M, Morice CP (2012) Hemispheric and large-scale land-surface air temperature variations: An extensive revision and an update to 2010. J Geophys Res 117:D05127. doi:10.1029/2011JD017139

Kalugin IA, Daryin AV, Babich VV (2009) Reconstruction of annual air temperatures for three thousand years in Altai region by lithological and geochemical indicators in Teletskoe Lake sediments. Dokl Earth Sci 426:681–684

Keppenne CL, Ghil M (1993) Adaptive filtering and prediction of noisy multivariate signals: An application to subannual variability in atmospheric angular momentum. Intl J Bifurcation Chaos 3:625–634

Kerr RA (2000) A North Atlantic climate pacemaker for the centuries. Science 288:1984–1986

Kimoto M, Ghil M (1993) Multiple flow regimes in the Northern Hemisphere winter. Part II: Sectorial regimes and preferred transitions. J Atmos Sci 50:2645–2673

Kitagawa H, Matsumoto E (1995) Climatic implications of δ^{13}O variations in a Japanese cedar (Cryptomeria japonica) during the last two millennia. Geophys Res Lett 22:2155–2158

Kobashi T, Kawamura K, Severinghaus JP, Barnola J-M, Nakaegawa T, Vinther BM, Johnsen SJ, Box JE (2011) High variability of Greenland surface temperature over the past 4000 years estimated from trapped air in an ice core. Geophys Res Lett 38:L21501. doi:10.1029/2011GL049444

Kobashi T, Shindell DT, Kodera K, Box JE, Nakaegawa T, Kawamura K (2013) On the origin of multidecadal to centennial Greenland temperature anomalies over the past 800 yr. Clim Past 9:583–596. doi:10.5194/cp-9-583-2013

Larsen DJ, Miller GH, Geirsdóttir Á (2013) Asynchronous Little Ice Age glacier fluctuations in Iceland and European Alps linked to shifts in subpolar North Atlantic circulation. Earth Planet Sci Lett 380:52–59

Lim J, Matsumoto E, Kitagawa H (2005) Eolian quartz flux variations in Cheju Island, Korea, during the last 6500 yr and a possible Sun-monsoon linkage. Quat Res 64:12–20

Lindholm M, Jalkanen R, Salminen H, Aalto T, Ogurtsov M (2011) The height-increment record of summer temperature extended over the last millennium in Fennoscandia. Holocene 21:319–326

Lindholm M, Jalkanen R (2012) Subcentury scale variability in height-increment and tree-ring width chronologies of Scots pine since AD 745 in northern Fennoscandia. Holocene 22:571–577

Liu Y, An ZS, Linderholm HW, Chen DL, Song HM, Cai QF, Sun JY, Tian H (2009) Annual temperatures during the last 2485 years in the mid-eastern Tibetan Plateau inferred from tree rings. Sci China Ser D 52:348–359

Liu Y, Cai QF, Song HM, An ZS, Linderholm HW (2011) Amplitudes, rates, periodicities and causes of temperature variations in the past 2485 years and future trends over the central-eastern Tibetan Plateau. Chin Sci Bull 6:2986–2994

Ljungqvist FC, Krusic PJ, Brattström G, Sundqvist HS (2012) Northern Hemisphere temperature patterns in the last 12 centuries. Clim Past 8:227–249

Lomb NR (1976) Least-squares frequency analysis of unequally spaced data. Astrophys Space Sci 39:447–462

Loso MG (2009) Summer temperatures during the Medieval Warm Period and Little Ice Age inferred from varved proglacial lake sediments in southern Alaska. J Paleolimnol 41:117–128

Lovejoy S, Schertzer D (2012) Stochastic and scaling climate sensitivities: Solar, volcanic and orbital forcings. Geophys Res Lett 39:L11702. doi:10.1029/2012GL051871

MacDonald GJ (1989) Spectral analysis of time series generated by nonlinear processes. Rev Geophys 27:449–469

Mangini A, Spötl C, Verdes P (2005) Reconstruction of temperature in the Central Alps during the past 2000 yr from a δ^{18}O stalagmite record. Earth Planet Sci Lett 235:741–751

Mann ME, Lees JM (1996) Robust estimation of background noise and signal detection in climatic time series. Clim Change 33:409–445

Mann ME, Zhang Z, Rutherford S, Bradley RS, Hughes MK, Shindell D, Ammann C, Faluvegi G, Ni F (2009) Global signatures and dynamical origins of the Little Ice Age and Medieval Climate Anomaly. Science 326:1256–1260

Marcus SL, Ghil M, Ide K (1999) Models of solar irradiance variability and the instrumental temperature record. Geophys Res Lett 26:1449–1452

Martín-Chivelet J, Muñoz-García MB, Edwards RL, Turrero MJ, Ortega AI (2011) Land surface temperature changes in Northern Iberia since 4000 yr BP, based on δ^{13}C of speleothems. Glob Planet Change 77:1–12

Masson-Delmotte V, Schulz M, Abe-Ouchi A, Beer J, Ganopolski A, González-Rouco JF, Jansen E, Lambeck K, Luterbacher J, Naish T, Osborn T, Otto-Bliesner B, Quinn T, Ramesh R, Rojas M, Shao X, Timmermann A (2013) Information from Paleoclimate Archives. In: Stocker, TF, Qin D, Plattner G-K, Tignor M, Allen SK, Boschung J, Nauels A, Xia Y, Bex V, Midgley PM (eds) Climate Change (2013): The Physical Science Basis. Contribution of Working Group I to the Fifth Assessment Report of the Intergovernmental Panel on Climate Change. Cambridge University Press, Cambridge

McKay NP, Kaufman DS, Michelutti N (2008) Biogenic silica concentration as a high-resolution, quantitative temperature proxy at Hallet Lake, south-central Alaska. Geophys Res Lett 35:L05709. doi:10.1029/2007GL032876

Moberg A (2013) Comparisons of simulated and observed Northern Hemisphere temperature variations during the past millennium. Selected lessons learned and problems encountered. Tellus B 65:19921. doi:10.3402/tellusb.v65i0.19921

Moore JJ, Hughen KA, Miller GH, Overpeck JT (2001) Little Ice Age recorded in summer temperature reconstruction from varved sediments of Donard Lake, Baffin Island, Canada. J Paleolimnol 25:503–517

Moron V, Vautard R, Ghil M (1998) Trends, interdecadal and interannual oscillations in global sea-surface temperatures. Clim Dyn 14:545–569

Percival DB, Walden AT (2000) Wavelet methods for time series analysis. Cambridge University Press, Cambridge

Naurzbaev MM, Vaganov EA, Sidorova OV, Schweingruber FH (2002) Summer temperatures in eastern Taimyr inferred from a 2427-year late-Holocene tree-ring chronology and earlier floating series. Holocene 12:727–736

Ogurtsov M, Sonninen E, Hilasvuori E et al (2010) Variations in tree ring stable isotope records from northern Finland and their possible connection to solar activity. J Atmos Sol Terr Phy 73:383–387

Ogurtsov M, Lindholm M, Jalkanen R, Veretenenko SV (2013) New evidence of solar variation in temperature proxies from Northern Fennoscandia. Adv Space Res 52:1647–1654

PAGES 2k Consortium (2013) Continental-scale temperature variability during the past two millennia. Nat Geosci 6:339–346

Plaut G, Vautard R (1994) Spells of low-frequency oscillations and weather regimes in the Northern hemisphere. J Atmos Sci 51:210–236

Press WH, Teukolsky SA, Vetterling WT, Flannery BP (2007) Numerical recipes: the art of scientific computing, 3rd edn. Cambridge University Press, Cambridge

Press WH, Rybicki GB (1989) Fast algorithm for spectral analysis of unevenly sampled data. ApJ 338:277–280

Raspopov OM, Dergachevb VA, Kolström T (2004) Periodicity of climate conditions and solar variability derived from dendrochronological and other palaeo-climatic data in high latitudes. Palaeogeogr Palaeoclimatol Palaeoecol 209:127–139

Raspopov OM, Dergachev VA, Esper J et al (2008) The influence of the de Vries ($\sim$200-year) solar cycle on climate variations: Results from the central Asian Mountains and their global link. Palaeogeorg Palaeoclimatol Palaeoecol 259:6–16

Salzer MW, Kipfmueller KF (2005) Reconstructed temperature and precipitation on a millennial timescale from tree-rings in the Southern Colorado Plateau, USA. Clim Change 70:465–487

Scargle JD (1982) Studies in astronomical time series analysis. II. Statistical aspects of unevenly spaced data. ApJ 263:835–853

Schlesinger ME, Ramankutty N (1994) An oscillation in the global climate system of period 65–70 years. Nature 367:723–726

Shabalova MV, Weber SL (1998) Seasonality of low-frequency variability in early instrumental European temperatures. Geoph Res Lett 25:3859–3862

Shabalova MV, Weber SL (1999) Patterns of temperature variability on multidecadal to centennial timescales. J Geophys Res 104:31023–31041

Sicre M-A, Jacob J, Ezat U, Rousse S, Kissel C, Yiou P, Eiríksson J, Knudsen KL, Jansen E, Turon J-L (2008) Decadal variability of sea surface temperatures off North Iceland over the last 2000 years. Earth Planet Sci Lett 268:137–142

Sicre MA, Hall IR, Mignot J, Khodri M, Ezat U, Truong M-X, Eiríksson J, Knudsen K-L (2011) Sea surface temperature variability in the subpolar Atlantic over the last two millennia. Paleoceanography 26:PA4218. doi:10.1029/2011PA002169

Siscoe GL (1978) Solarterrestrial influences on weather and climate. Nature 276:348–352

Sleptsov AM, Klimenko VV (2003) Multi-proxy reconstruction of the climate of Eastern Europe during the last 2,000 years. Izvestya Russ Geograph Soc 6:45–54 [in Russian]

Springer GS, Rowe HD, Hardt B, Edwards RL, Cheng H (2008) Solar forcing of Holocene droughts in a stalagmite record from West Virginia in east-central North America. Geophys Res Lett 35:L17703. doi:10.1029/2008GL034971

Steinhilber F, Abreu JA, Beer J, Brunner I, Christl M, Fischer H, Heikkilä U, Kubik W, Mann M, McCracken KG, Miller H, Miyahara H, Oerter H, Wilhelms F: 9,400 years of cosmic radiation and solar activity from ice cores and tree rings. Proc Natl Acad Sci 109:5967–5971

Støve B, Ljungqvist FC, Thejll P (2012) A test for nonlinearity in temperature proxy records. J Clim 25:7173–7186

Sutton RT, Hodson DL (2005) Atlantic Ocean forcing of North American and European summer climate. Science 309:115–118

Tan M, Liu TS, Hou J, Qin X, Zhang H, Li T (2003) Cyclic rapid warming on centennial-scale revealed by a 2650-year stalagmite record of warm season temperature. Geophys Res Lett 30:1617–1620. doi:10.1029/2003GL017352

Tingley MP, Craigmile PF, Haran M, Li B, Mannshardt E, Rajaratnam B (2012) Piecing together the past: statistical insights into paleoclimatic reconstructions. Quat Sci Rev 35:1–22

Torrence C, Compo GP (1998) A practical guide to wavelet analysis. B Am Meteorol Soc 79:61–78

Unal YS, Ghil M (1995) Interannual and interdecadal oscillation patterns in sea level. Clim Dyn 11:255–278

Van Loon H, Rogers JC (1978) The seesaw in winter temperatures between Greenland and northern Europe, Part I: General description. Mon Wea Rev 106:296–310

Vautard R, Yiou P, Ghil M (1992) Singular spectrum analysis: a toolkit for short noisy chaotic signals. Phys D 58:95–126

Vautard R, Ghil M (1989) Singular spectrum analysis in nonlinear dynamics, with applications to paleoclimatic time series. Phys D 35:395–424

Velasco VM, Mendoza B (2008) Assessing the relationship between solar activity and some large scale climatic phenomena. Adv Space Res 42:866–878

Venegas SA (2001) Statistical methods for signal detection in climate. Technical Report,Danish Center for Earth System Science, DCESS Report No. 2

Yang B, Braeuning A, Johnson KR, Yafeng S (2002) General characterisics of temperature variation in China during the last two millennia. Geophys Res Lett 29:1324. doi:10.1029/2001GL014485

Yu Z, Ito E (1999) Possible solar forcing of century scale drought frequency in the northern Great Plains. Geology 27:263–266

Wagner G, Beer J, Masarik J et al (2001) Presence of the solar de Vries cycle (∼205 years) during the last ice age. Geophys Res Lett 28:303–306

Wang J, Yang B, Ljungqvist FC, Zhao Y (2013) The relationship between the Atlantic Multidecadal Oscillation and temperature variability in China during the last millennium. J Quat Sci 28:653–658

Wanner H, Beer J, Bütikofer J, Crowley T, Cubasch U, Flückiger J, Goosse H, Grosjean M, Joos F, Kaplan JO, Küttel M, Müller S, Pentice C, Solomina O, Stocker T, Tarasov P, Wagner M, Widmann M (2008) Mid to late Holocene climate change: an overview. Quat Sci Rev 27:1791–1828

Weare BC, Nasstrom JN (1982) Examples of extended empyrical orthogonal function analyses. Mon Wea Rev 110:481–485

Wiles GC, D'Arrigo RD, Villalba R, Calkin PE, Barclay DJ (2004) Century-scale solar variability and Alaskan temperature change over the past millennium. Geophys Res Lett 31:L15203. doi:10.1029/2004GL020050

Willard DA, Bernhardt CE, Korejwo DA, Meyers SR (2005) Impact of millennial-scale Holocene climate variability on eastern North American terrestrial ecosystems: pollen-based climatic reconstruction. Glob Planet Change 47:17–35

Wilson R, Wiles G, D'Arrigo R, Zweck C (2007) Cycles and shifts: 1,300 years of multi-decadal temperature variability in the Gulf of Alaska. Clim Dyn 28:425–440